POLITECNICO DI TORINO
Repository ISTITUZIONALE

TeraHertz Vibrations and Phono-Fission Reactions from Crushing of Iron-rich Natural Rocks

Original
TeraHertz Vibrations and Phono-Fission Reactions from Crushing of Iron-rich Natural Rocks / Carpinteri, A., Borla, O., Lucia, U., Zucchetti, M.. - In: JOURNAL OF CONDENSED MATTER NUCLEAR SCIENCE. - ISSN 2227-3123. - STAMPA. - 37:1(2023), pp. 84-97.

Availability:
This version is available at: 11583/2982672 since: 2023-10-02T13:35:39Z

Publisher:
The International Society for Condensed Matter Nuclear Science ISCMNS

Published
DOI:

Terms of use:

This article is made available under terms and conditions as specified in the corresponding bibliographic description in the repository

Publisher copyright

(Article begins on next page)

27 October 2026

Computers and Chemical Engineering 216 (2027) 109892

Contents lists available at ScienceDirect

Computers and Chemical Engineering

journal homepage: www.elsevier.com/locate/compchemeng

Integrated multi-mechanism degradation modeling of a catalyst-coated membrane in a PEM electrolysis cell operating under renewable-powered conditions

Hossein Asgharian [a,*], Hamilton Delaney Miller [a], Florin Iov [a], Mads Pagh Nielsen [a], Alessandro Hugo Antonio Monteverde [b], Vincenzo Liso [a]

[a] Department of AAU Energy, Aalborg University, Pontoppidanstræde 111, Aalborg, 9220, Denmark
[b] Politecnico di Torino, Department of Applied Science and Technology, Corso Duca degli Abruzzi 24, Torino, 10129, Italy

ARTICLE INFO

Keywords:
Green hydrogen production
Degradation mechanisms
PEM electrolysis cell
Voltage degradation
Catalyst coated membrane

ABSTRACT

Green hydrogen from water electrolysis is key to producing electro-fuels for decarbonizing aviation and maritime transport. PEM electrolysis systems offer an efficient and high-purity solution powered by renewable energy. This study modeled a proton exchange membrane (PEM) electrolysis cell and evaluated its performance, accounting for key degradation mechanisms within the catalyst coated membrane (CCM): membrane thinning, iridium dissolution in the anode electrode, and platinum crystallite agglomeration in the cathode electrode. The results indicated that after 20,000 h (2.283 years) of operation, membrane thinning was the primary factor limiting the cell lifetime, increasing the overpotentials and power consumption. It was also observed that increasing the current density of the PEM electrolysis cell from 1 $A.cm^{-2}$ to 2 $A.cm^{-2}$ leads to a decrease in cell efficiency and an accelerated degradation rate, resulting in a 27% reduction in lifetime and a 1.78-fold increase in voltage degradation. This study also examined the effects of operating temperature and pressure on cell degradation. Reducing the cell temperature from 80 °C to 70 °C decreased efficiency by 0.64% at the beginning of life (BOL) by increasing the overpotentials. However, this reduction in operating temperature resulted in reduced degradation, leading to 8.18% higher efficiency after 20,000 h of operation. This study also investigated the effects of idle operation and pressure on the degradation of the CCM and identified the operating condition offering the most favorable durability–efficiency trade-off among the evaluated operating conditions.

1. Introduction

Aviation and maritime sectors are among the hardest sectors to decarbonize. To decarbonize these sectors, it is necessary to generate hydrogen and electro-fuels effectively at low costs. In addition to their role in decarbonizing the hard-to-abate sectors, electro-fuels can also serve as a means of energy storage. In this scenario, when renewable energy is abundant, the surplus power can be used to generate hydrogen via electrolysis for electro-fuel production. The resulting electro-fuels, such as methanol or ammonia, can be conveniently stored and later utilized in combustion engines when renewable electricity is unavailable. It is important to note that green hydrogen production remains the most challenging step in electro-fuel generation due to the high power demand and substantial capital costs associated with the water electrolysis process (Paulsen et al., 2024).

Hydrogen can be produced from water using alkaline electrolysis (AEL) systems, PEM electrolysis systems, and solid oxide electrolysis systems (SOECs). AEL systems are well-established, cost-effective, and commercially available (Valverde-Isorna et al., 2016). However, they exhibit relatively low energy efficiency, produce hydrogen of lower purity, and are less compatible with intermittent renewable energy sources due to their slower dynamic response to fluctuations in power supply (Haoran et al., 2024). SOECs, on the other hand, offer superior energy efficiency, high current density in the electrolysis process, excellent reliability, and a unit-based design (Tian et al., 2022). Nevertheless, they suffer from high-temperature operating ranges, slow dynamic response under varying renewable power, and significant degradation of material (Xu et al., 2024). In contrast, PEM electrolysis systems provide several advantages, including elevated energy efficiency, rapid response to power variations, operation at reduced temperatures, space-efficient design, and high current density (Kumar and

* Corresponding author.
E-mail address: hoas@energy.aau.dk (H. Asgharian).

https://doi.org/10.1016/j.compchemeng.2026.109892
Received 26 January 2026; Received in revised form 28 July 2026; Accepted 8 September 2026
Available online 10 September 2026
0098-1354/© 2026 The Author(s). Published by Elsevier Ltd. This is an open access article under the CC BY license (http://creativecommons.org/licenses/by/4.0/).

Nomenclature

A	Surface area (m^2)
a	Water activity [-], Surface-area-to-volume ratio (m^{-1})
c	Concentration ()
CCM	Catalyst coated membrane
D	Diffusivity coefficient (m^2/s)
d_M	Crystallite diameter of the catalyst material (nm)
E	Activation energy (J/mol)
E^0	Reversible cell voltage (V)
e_{clC}	Thickness of the electrode (μm)
EW	Equivalent weight (g/mol)
F	Faraday constant (C/mol)
G_d	Molar flux of water due to diffusion (mol/s)
G_{eo}	Water drag flux inside the membrane (mol/s)
i	Current density (A/cm^2)
I	Current (A)
i_0^*	Specific exchange current density (A/cm^2)
c	Concentration (mol/m^3)/(mol/l)
k	Kinetic constant
l	Loading (mg)
M	Molar mass (g/mol)
m_M	catalyst loading on the cathode side (g/cm^2)
$\dot{m}$	Variation of iridium loading with the time (mg/s)
n_d	Drag coefficient [-]
$\dot{N}$	Molar flow rate (mol/s)
P	Pressure (bar)
r	Area-specific ohmic resistance ($\Omega.cm^2$), radius of crystallite (m)
R	Gas constant (J/(mol.K))
S	Solubility ($mol/(m^3.bar)$)
t	Membrane thickness (cm/m)
T	Temperature (K)
v, V	Reaction rate ($mol/(m^3.s)$), Stoichiometric coefficient [-], velocity of water (m/s), atomic volume (m^3/atom)
x	Mole fraction [-]
z	Number of moles of transferred electrons [-]

Greek letters

ϕ	Crossover (mol/s)
ϕ_I	Fraction of the metal catalyst available at the surface [-]
ε	Dimensionless factor
λ	Water content in the membrane [-]
ρ	Density (gr/l)
γ_M	Roughness [-]
δ	Constant coefficient with value of 0 or 1
η	Over potential (V)
σ	Proton conductivity (S/cm)
α_{an}	Constant coefficient [-]
γ	Surface energy (J/m^2)
Ω	Molar volume (m^3/mol)

Subscripts

an	Anode
act	Activation
ca	Cathode
Con	Concentration
diss	Dissolution
eff	Effective
el	Electrolysis cell
M, mem	Membrane
OC	Open circuit
ref	Reference
sat	Saturation
w	Water
0	Initial stage
Pt	Platinum
B	Boltzmann
atom	Atomic

Abbreviation

BOL	Beginning of life
ECSA	Electrochemical active surface area (cm^2/mg)
EOL	End of life
FRR	Fluoride Release Rate (μg/(hr.cm^2))
HHV	Higher heating value (J/mol)
LC	Load cycling
OER	Oxygen evolution reaction
PEM	Proton exchange membrane
TR	Thinning rate (nm/hour)

Himabindu, 2019). These characteristics make PEM technology particularly attractive for green hydrogen production and electro-fuel generation. However, like AEL and SOECs, PEM electrolysis systems also experience performance degradation during operation, making it essential to evaluate the key factors contributing to their degradation.

The degradation of PEM electrolysis systems has been extensively investigated through experimental studies. Frensch et al. (2019) evaluated the performance of a PEM electrolysis system under various operating modes, including fixed voltage, fixed current at a wide range of temperatures, and cyclic current, to assess their impact on degradation. Their results demonstrated that faster cycling of cell current density led to better cell performance over 500 h of operation. Similarly, Tejera et al. (2024) also examined PEM electrolysis cell degradation with a focus on the membrane–electrode assemblies (MEAs), using a cell with a 25 cm^2 active area and a catalyst loading of 3 $mg.cm^{-2}$, employing N1110 as membrane. The cell was operated at 2 V and 60 °C for 168 h, and electrochemical techniques such as electrochemical impedance spectroscopy, linear polarization curves, and chronoamperometry were used to assess stability. Their results indicated that degradation was primarily due to reversible contamination, and that acidic treatment partly recovered the productivity, reducing the rate of degradation to 40 $\mu A.h^{-1}.cm^{-2}$. Rakousky et al. (2016) conducted a 1000-hour experimental stability study on a single PEM electrolysis cell and reported a degradation rate of approximately 194 μV h^{-1}, with rising ohmic overpotentials accounting for over 78% of the observed degradation. Grigoriev et al. (2014) performed a detailed investigation focusing on catalyst dissolution at the anode side and decrease in thickness of membrane. Using platinum as the catalyst on both electrodes, they identified the MEA as the most vulnerable element in the PEM electrolysis unit, ultimately limiting its lifetime. Their results revealed that catalyst layer corrosion and its relocation into the membrane were the primary degradation mechanisms, and the membrane lost nearly 75% of its thickness after 5500 h of operation.

Several models have been developed to study specific degradation mechanisms in PEM electrolysis cells without the need to run long-term experiments. Dominguez et al. (2025) developed a time-dependent multiscale model to investigate the reliability of the electrode material on the anode side under varying performance conditions, particularly when using reduced loadings of noble metal. This approach significantly decreased the computational cost of modelling the cell over extended periods of operation. However, their results showed that while the model offered faster simulations, it did not align well with experimental data under triangular and sawtooth dynamic current profiles. Kalinnikov et al. (2023) proposed a physicochemical model to

investigate the dissolution of iridium when used as the anodic catalyst material. Their study assessed iridium consumption across various current densities, anode transport layer thicknesses, and operating pressures. They reported that higher current densities led to increased iridium dissolution, whereas operating pressure and variations in anode transport layer thickness (within the 25–200 μm range) had negligible effects. Chandesris et al. (2015) focused on modeling the temporal reduction in membrane thickness and its associated degradation in PEM electrolysis systems. They provided a detailed mechanistic framework describing 10 key reactions involved in membrane thinning, along with their rate constants and reaction rates. Furthermore, they derived analytical expressions for the concentrations of reactive species, including H_2O_2, $H\dot{O}$, $H\dot{O}O$, Fe^{2+}, and Fe^{3+} in order to evaluate how membrane thickness decreases over time due to radical attack in a PEM electrolysis cell.

Although PEM electrolysis systems for green hydrogen production are expected to reach capacities of hundreds of gigawatts by 2030 (Wang et al., 2025), comprehensive studies on the performance evaluation and degradation mechanisms of PEM electrolysis stacks remain limited. As shown in Fig. 1, a PEM electrolysis stack is subjected to stack input variables including current (with ripple components), load cycling (LC), idle operation, and pressure. The distribution of current and pressure among individual cells may be non-uniform. Therefore, these parameters are referred to as stack-level input variables, while the corresponding inputs for each cell are defined as cell-level input variables. In PEM electrolysis systems, water serves both as the reactant for hydrogen production and as a cooling medium, typically defined by a water-to-hydrogen stoichiometry coefficient in the range of 95–1035 (Panchenko et al., 2019). Consequently, accurate assessment of thermal management, including the different heat transfer and heat removal mechanisms shown in Fig. 1, is essential, as temperature variations between cells can significantly influence the performance and durability. In particular, inner cells within the stack tend to operate at higher temperatures, whereas outer cells adjacent to the end plates remain comparatively cooler, as reported in (Kimmel et al., 2025). However, a comprehensive modelling framework that captures stack degradation under these coupled effects and enables prediction of voltage degradation (as a stack output variable) has not yet been established. Consequently, it is essential to develop a detailed degradation model at the PEM electrolysis cell level, particularly focusing on the CCM under ideal current supply conditions, as illustrated by the dashed boundaries in Fig. 1, and subsequently extend this model to the stack level to enable a thorough evaluation of stack degradation and performance. Although several models have been developed to study anode catalyst dissolution and membrane thinning, to the best of our knowledge, no holistic model exists that simultaneously evaluates multiple degradation mechanisms in PEM electrolysis cells, including membrane thinning, platinum agglomeration as cathode catalyst material, and dissolution of iridium as anode catalyst material. This study presents, for the first time, a comprehensive model to investigate how the overpotential and energy efficiency of a PEM electrolysis cell evolve over time as a result of CCM degradation under both constant and variable load conditions. Furthermore, this study evaluates the effects of current density applied to the cell, idle operation, cell operating temperature and pressure on performance, energy efficiency, and the resulting degradation.

2. Model description

A dynamic model of the PEM electrolysis cell, including its degradation, was developed in MATLAB R2024a. The model incorporates the cathode, anode, and membrane compartments and accounts for the main degradation mechanisms identified in literature. Specifically, it considers dissolution of iridium as the anode-side catalyst material, agglomeration of platinum crystallite as the cathode-side catalyst material, and membrane thinning, as illustrated in Fig. 2, to evaluate the CCM degradation under both constant and variable load conditions. It is worth noting that the chemical degradation of the PEM electrolysis cell due to membrane thinning was modeled and evaluated using the kinetic expressions for calculating the concentrations of key species (H_2O_2, $H\dot{O}$, $H\dot{O}O$, Fe^{2+}, and Fe^{3+}), as discussed in Section 2.3.

2.1. Main assumptions

This section outlines the key assumptions adopted in this study for modeling the degradation of the PEM electrolysis cell with focus on CCM. It also provides the corresponding justifications, rationale and references for each assumption.

2.1.1. Constant temperature

A constant and uniform temperature distribution was assumed throughout the electrolysis cell. Heat generated during the operation was assumed to be effectively dissipated through heat transfer mechanisms that were not explicitly considered, as thermal management was beyond the scope of this study.

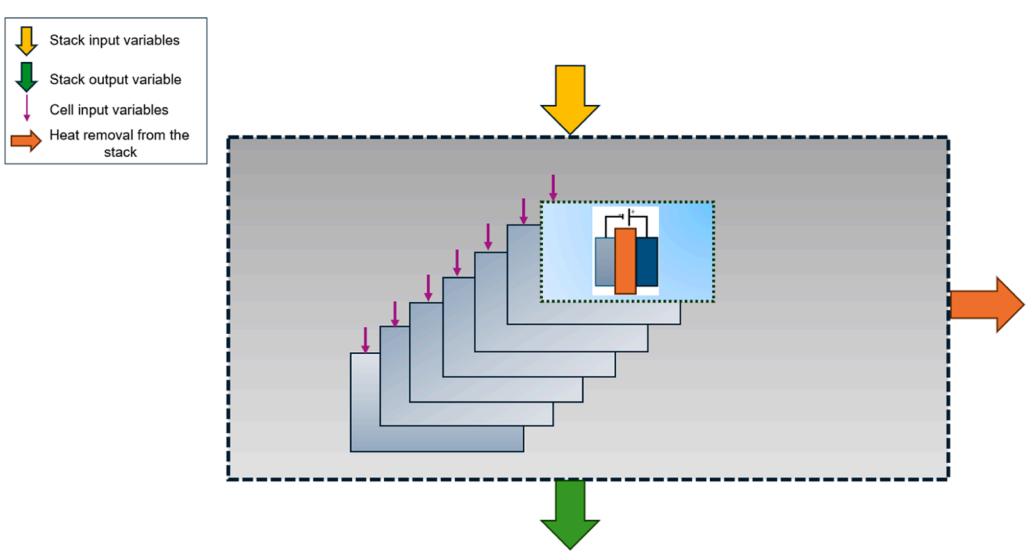

Fig. 1. Illustration of stack-level and cell-level input and output variables and associated heat removal mechanisms from the stack.

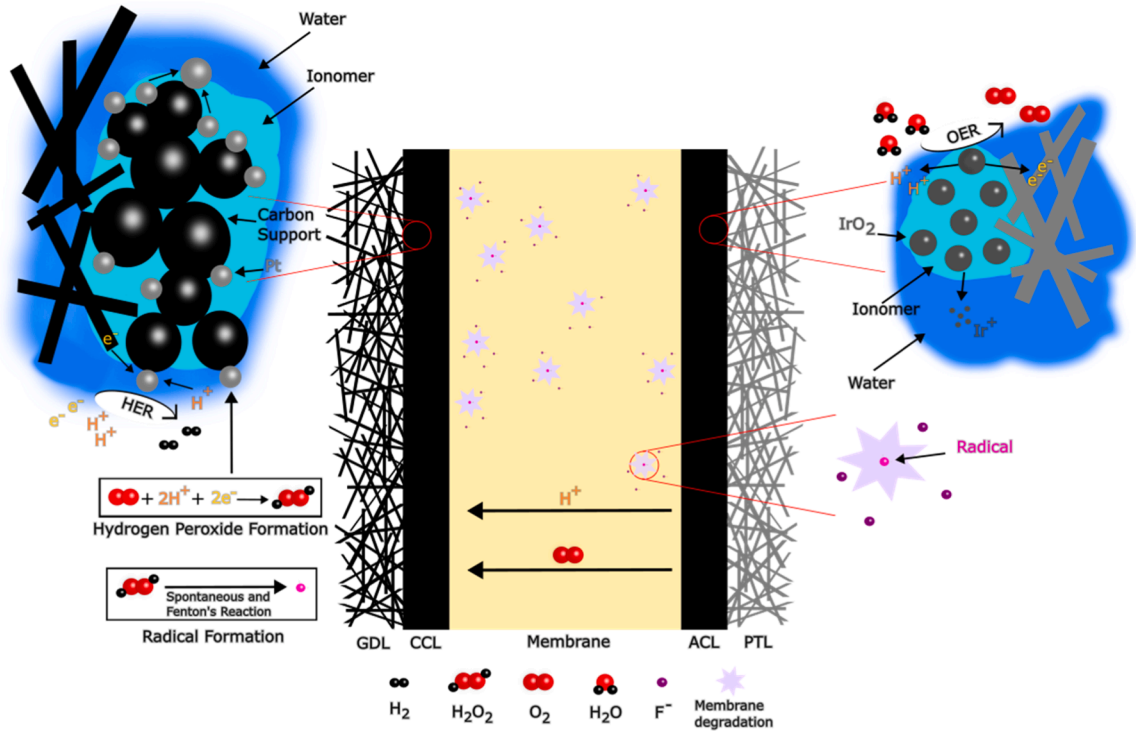

Fig. 2. Main degradation mechanisms considered and evaluated in this study.

2.1.2. Constant pressure

A constant operating pressure of 1 bar was assumed throughout the electrolysis cell. Consequently, pressure drops across the flow channels, porous transport layers, catalyst layers, and membrane were neglected in the present model. Hence, this study does not investigate cavitation erosion associated with gas bubbles. Cavitation erosion is typically caused by the violent collapse of bubbles, which generates strong shock waves capable of damaging material surfaces (Zhao et al., 2025). Such a phenomenon is unlikely to occur in the PEM electrolysis cell considered in this study. This is primarily because the violent collapse of oxygen bubbles requires the external pressure to be significantly higher than the pressure inside the bubbles. Such conditions are inconsistent with the assumption of a constant pressure throughout the electrolysis cell adopted in the present model.

2.1.3. Ramp rate

This study assumes that the power input to the PEM electrolysis cell can be varied instantaneously, as the system exhibits a high ramp rate of approximately 90%/s, as reported in Wang et al. (2025). Consequently, dynamic limitations associated with slower load response were not considered in this work.

2.1.4. Water molar fraction of unity on the anode side

It was assumed that the ratio of gas production on the anode side to the available water, which acts both as reactant and cooling medium, is sufficiently low. Therefore, the water molar fraction was taken as unity on the anode side, in accordance with (Medina and Santarelli, 2010).

2.1.5. Platinum dissolution on the cathode side

This study neglects the dissolution of the platinum catalyst at the cathode of the PEM electrolysis cell. According to (Dodwell et al., 2021), platinum dissolution occurs primarily under open-circuit voltage conditions at extremely low rates (approximately 0.005% over 90 h of operation) and decreases to negligible values once current is applied to the cell.

2.1.6. Iridium agglomeration on the anode side

The agglomeration of the Ir catalyst at the anode electrode is not considered in this study. According to (Rakousky et al., 2016) no agglomeration of Ir was observed during the 1150 h of PEM electrolysis operation.

2.1.7. Constant surface area to volume ratio

This study assumes a constant surface-area-to-volume ratio when modelling the dissolution of Ir used as the catalyst material over the anode electrode. This assumption is based on the information provided in (García-Salaberri et al., 2025; De Angelis et al., 2023), which relates the anode electrode thickness to Ir loading using a linear relationship.

2.1.8. Ideal gas

This assumption was made to simplify the calculation of gas activities used in determining the open-circuit overpotential in Eq. (54). This assumption was made based on the information provided in Saidi et al. (2025).

2.1.9. Ideal DC current supply

This study assumes an ideal current supply and neglects the transients and ripples generated during the conversion of alternating current (AC) to direct current (DC), as the focus is on the performance and degradation of a single PEM electrolysis cell. Such transient effects would become more relevant when modeling large-scale stacks operating at the MW scale.

2.1.10. Hot and cold shutdowns and start ups

Although this study considers degradation associated with idle operation resulting from the intermittent nature of renewable power supply, it does not account for the stress and degradation induced by hot and cold start–stop cycles. While such operating conditions may induce mechanical and electrochemical stress in PEM electrolysis units, their impact is assumed to be exceedingly low based on the information provided in Gladik et al. (2025), as long as the correct start–stop procedures are followed.

2.1.11. Stability number

This study assumes that expressions used for the S_{number} are valid over extended operating time as it has been mentioned in Dam et al. (2025) that the expression given by Eq. (25) for the S_{number} was valid over 1000 h of operation. Hence, this study also assumed that the expression used for this parameter in Eq. (25) is valid for extended operating periods (until EOL and throughout 20,000 h of operation). Additionally, based on the data and trends reported in Milosevic et al. (2026), this study assumes that the variation of S_{number} over time under idle operation can be predicted using Eq. (64). This assumption is not expected to significantly affect the results because, according to the data presented in Milosevic et al. (2026), the parameter exhibits a rapid increase during the initial stage of operation, after which its rate of change becomes minimal. Consequently, employing the correlation for S_{number} given in Eq. (64) over the entire operating period is considered a reasonable approximation.

2.1.12. Impact of measurement uncertainties on cell degradation

In practice, laboratory measurement instruments are not ideal and are associated with inherent uncertainties and measurement errors. However, this study has not been designed to account for these uncertainties in measured variables such as cell temperature, pressure, and current, nor does it investigate their potential impact on predicted cell performance and degradation.

2.1.13. Surface morphology due to Ir dissolution

It is worth noting that, although Ir dissolution affects the surface morphology and local current distribution at the anode, a comprehensive analysis of the resulting morphology evolution based on structural shape and texture changes of the anode's outer layer would require multiscale modeling across the micro-, meso-, and macroscale (Liu et al., 2025). Such an approach is beyond the scope of this study. Therefore, this study focuses on developing a simplified yet physically consistent mathematical model to describe the exchange current density of the anode electrode as a function of Ir loading during its dissolution in the acidic environment of a PEM electrolysis unit. The model is then used to calculate the temporal evolution of anodic overpotential as a consequence of CCM degradation induced by Ir dissolution.

2.1.14. Ideal membrane hydration

This study assumes that the membrane in the PEM electrolysis cell remains ideally hydrated and, therefore, does not consider the effects of membrane drying or dehydration. Membrane dehydration may occur primarily due to excessively high operating temperatures (>100 °C) and insufficient water supply at the anode side (Kuhnert et al., 2023). However, these conditions are unlikely to occur under the operating conditions considered in this study, which involve temperatures up to 80 °C, adequate heat removal, and sufficient water supply at the anode side. Membrane dehydration can result in reduced proton conductivity, decreased membrane water uptake, and lower electrolysis cell efficiency.

2.2. Modelling of the anode chamber

On the anode side of the PEM electrolysis cell, oxygen and protons are produced from water according to the following reaction:

$$2H_2O \rightarrow O_2 + 4H^+ + 4e^- \tag{1}$$

The flow rate of the generated oxygen can be calculated using Faraday's law as follows:

$$\dot{n}_{O_2}^{gen} = \frac{iA}{4F} \tag{2}$$

Eq. (3) represents the molar flow balance of oxygen on the anode side of the PEM electrolysis cell. It accounts for the oxygen inlet and outlet fluxes in the anode chamber, as well as the molar flow rate of generated oxygen and the oxygen crossover to the cathode side (Sorace, 2021).

$$\frac{dN_{an,O_2}}{dt} = \dot{N}_{an,O_2}^{in} - \dot{N}_{an,O_2}^{out} + \dot{N}_{O_2}^{gen} - \dot{N}_{O_2}^{perm} \tag{3}$$

The last term in Eq. (3) can be calculated as follows:

$$\dot{N}_{O_2}^{perm} = \phi_{O_2}^{diff} + \phi_{O_2}^{drag} \tag{4}$$

The diffusion and electro-osmotic drag contributions to oxygen crossover shown in Eq. (4) can be expressed in mol/s as follows (Schalenbach et al., 2013):

$$\phi_{O_2}^{diff} = \frac{D_{O_2}.S_{O_2}.A_{cell}.P_{O_{2,\ an}}}{t} \tag{5}$$

$$\phi_{O_2}^{drag} = \frac{iA}{F} n_d \frac{S_{O_2} P_{O_{2,\ an}}}{c_{H_2O}} \tag{6}$$

It is worth noting that the partial pressure of oxygen on the cathode side is neglected in Eq. (5). In Eq. (6), n_d and c_{H_2O} represent the drag coefficient and the molar concentration of water. The partial pressure of oxygen on the anode side and the drag coefficient used in Eqs. (5) and 6 can be calculated using the following relations (Schalenbach et al., 2013; Stull; Lisoet al., 2018):

$$\begin{aligned} P_{O_{2,\ an}} &= P_{an} - P_{H_2O,\ sat}(T) \\ &= P_{an} - 611 \times 10^{-5}\ exp\left(5423\left(\frac{1}{273.15} - \frac{1}{T}\right)\right) \end{aligned} \tag{7}$$

$$n_d = 0.0134T + 0.03 \tag{8}$$

The coefficients in Eq. (5) can be determined as follows:

$$D_{O_2} = D_{O_2,0} \exp\left(\frac{-E_{A,O_2}}{RT}\right) \tag{9}$$

$$S_{O_2} = 0.55 \exp\left(A_{O_2} + \frac{B_{O_2}}{T} + C_{O_2} \ln\left(\frac{T}{100}\right)\right) \tag{10}$$

where $D_{O_2,0}$ and E_{A,O_2} denote the pre-exponential factor and activation energy, respectively, while A, B and C are constants. The values of $D_{O_2,0}$, E_{A,O_2} and these constants are provided in Table 1.

The molar flow balance of water in the anode chamber is calculated using Eq. (11), accounting for water inlet and outlet, water consumption, and water transport through the membrane (Sorace, 2021):

$$\frac{dN_{an,H_2O}}{dt} = \dot{N}_{an,H_2O}^{in} - \dot{N}_{an,H_2O}^{out} + \dot{N}_{H_2O}^{cons} - \dot{N}_{H_2O}^{mem} \tag{11}$$

An iterative approach was employed to calculate the amount of water crossing the membrane. In this calculation, both electro-osmotic drag and water diffusion were considered, while hydraulic transport was neglected, as the anode and cathode operate at atmospheric pressure. To determine water transport via electro-osmotic drag, the drag coefficient, which represents the number of moles of water transported per mole of proton, is calculated as a function of membrane temperature as follows (Onda et al., 2002):

$$n_{d,w} = 0.0134T_m + 0.03 \tag{12}$$

The amount of water transported within the membrane due to

Table 1
Parameters applied to calculate oxygen solubility and diffusivity (Fahr et al., 2024).

Parameters	Value	Unit
$D_{O_2,0}$	4.2×10^{-6}	m^2/s
E_A	18,380	J/mol
A	−66.73538	-
B	8747.547	K
C	24.45264	-

electro-osmotic drag is calculated as follows (Medina and Santarelli, 2010):

$$G_{eo} = n_{d,w}\frac{i}{F}A \tag{13}$$

The molar flux of water due to diffusion is also determined as follows:

$$G_d = D_{eff}\frac{(C_{an} - C_{ca})}{t_m}A \tag{14}$$

where C_{an} and C_{ca} represent the water concentrations at the anode and cathode, respectively. The effective diffusion coefficient, D_{eff}, is given by the following equation:

$$D_{eff} = \varepsilon^{1.5}D_w \tag{15}$$

where ε is a dimensionless factor with a value of 0.3, and D_w is the water diffusion coefficient, which can be calculated as follows:

$$D_w = 0.256 \times 10^{-4}\left(\frac{T_{cell}}{273.15}\right)^{1.823} \tag{16}$$

The water concentrations at the cathode and anode can also be calculated using the following equations:

$$C_{an} = \frac{\rho_{m,dry}\lambda_{an}}{M_{m,dry}} \tag{17}$$

$$C_{ca} = \frac{\rho_{m,dry}\lambda_{ca}}{M_{m,dry}EW} \tag{18}$$

where λ_{an} and λ_{ca} represent the water content on the anode and cathode sides, respectively. These parameters are calculated from water activity as follows:

$$\lambda = 0.043 + 17.81a - 39.85a^2 + 36a^3,\ 0 < a \leq 1 \tag{19}$$

$$\lambda = 14 + 1.4(a-1)^3,\ 1 < a < 3 \tag{20}$$

$$a = x_w\frac{P}{P_{sat}} \tag{21}$$

where x_w represents the molar fraction of water, which is approximately 1 on the anode side, while its value on the cathode side can be calculated using the following equation:

$$x_w = \frac{\dot{n}_w}{\dot{n}_w + \frac{iA}{2F}} \tag{22}$$

In Eq. (22), $\dot{n}_w$ represents the total molar flow rate of water transported from the anode to the cathode, which can be calculated using the following equation:

$$\dot{n}_w = G_{eo} + G_d \tag{23}$$

It is worth noting that assuming a water molar fraction of unity on the anode side results in a water activity of 1.82 and a corresponding membrane water content of 14.77 close to the anode side, as calculated using Eqs. (19) and 20. On the other hand, an iterative method was employed in this study to determine the water molar fraction on the cathode side and, consequently, the water concentration required to calculate the molar flow rate of water transported by diffusion. Using this approach, a water activity of 1.11 and a water content of 14 were obtained for the cathode side. These values indicate that the membrane is fully hydrated on both the anode and cathode sides. Fig. 3 illustrates the variation in membrane proton conductivity and the corresponding ohmic overpotential of the membrane as a function of membrane water content. As shown, an increase in water content leads to higher proton conductivity and a reduction in the membrane ohmic overpotential. Thus, the membrane on the cathode side exhibits a higher ohmic overpotential than on the anode side due to its lower water content.

The acidic environment on the anode side reduces the stability of the iridium-based catalyst due to iridium dissolution during the oxygen evolution reaction (OER) (Geuß et al., 2024). This study models the iridium dissolution process and examines its effect on the anodic overpotential in a PEM electrolysis cell. Catalyst degradation is quantified using the stability number (S_{number}), defined as the ratio of oxygen generated through OER, calculated via Faraday's law at the anode, to the amount of iridium dissolved, as expressed below (Geuß et al., 2024):

$$S_{number} = \frac{n(O_2)}{n(Ir)} \tag{24}$$

The dependence of the S_{number} on current density is expressed by the

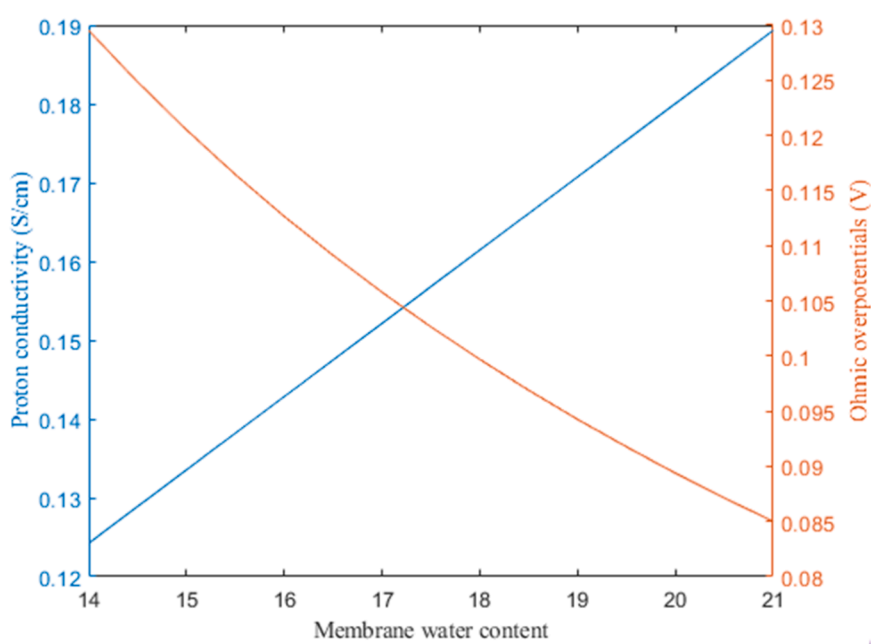

Fig. 3. Variation of proton conductivity and ohmic overpotential of membrane as a function of membrane water content.

following equation, which is valid for current densities in the range of 0–3 A.cm^{-2} (Dam et al., 2025):

$$S_{number} = \frac{1}{2.23 \times 10^{-10} i + 4.17 \times 10^{-10}} \tag{25}$$

According to Eq. (25), higher current densities result in lower stability numbers, which in turn lead to higher Ir dissolution rates. Operation of the PEM electrolysis unit at higher current densities increases the rate of proton generation, leading to a more acidic environment at the anode and consequently accelerating Ir dissolution. However, this study does not explicitly resolve the local proton concentration or the spatial evolution of pH on the anode side of the PEM electrolysis cell. Instead, their effects are indirectly accounted through the empirical correlation adopted in Eq. (25) to determine the S_{number}. The dissolution reaction rate, expressed in mg/s, can be determined from Eq. (26), which is derived by rearranging Eq. (24) and applying Faraday's law, as follows:

$$\dot{m}_{Ir,\ diss} = \frac{1000.i.A.M_{Ir}}{n.F.S_{number}} \tag{26}$$

where n represents the number of electrons transferred per mole of oxygen produced. As noted earlier, iridium dissolution decreases the catalyst active area on the anode, thereby reducing the specific electrochemical active surface area (ECSA) in the unit of cm^2/mg, lowering the apparent exchange current density, and consequently increasing the anodic overpotential. The reduction of ECSA and apparent exchange current density due to iridium dissolution can be expressed as follows (Rogler et al., 2025):

$$i_{0,a} = i_{0,s} l_{Ir} ECSA \tag{27}$$

where $i_{0,s}$ and l_{Ir} denote the specific exchange current density and iridium loading, respectively. The variation of iridium loading with time can be calculated using the following equation:

$$\frac{dl_{Ir}}{dt} = -\frac{\dot{m}_{Ir,\ diss}}{A} \tag{28}$$

The ECSA used in Eq. (27) can be calculated using the following equation (De Angelis et al., 2023):

$$ECSA = \frac{a t_{cat}}{l_{Ir}} \tag{29}$$

where a and t_{cat} represent the surface-area-to-volume ratio and the electrode thickness, respectively. Although a reduction in iridium loading due to iridium dissolution decreases both of these parameters, this study assumes that the surface-area-to-volume ratio remains constant (with value of 3.61 × 10^{-6} m^{-1} as reported in (De Angelis et al., 2023)), while the electrode thickness decreases as the iridium loading is reduced. The electrode thickness can therefore be expressed as a function of iridium loading using the following equation (García-Salaberri et al., 2025):

$$t_{cat} = 6.25 l_{Ir} \tag{30}$$

Hence, Eq. (27) can be reduced to the following equation:

$$i_{0,a} = 6.25 i_{0,s} a l_{Ir} \tag{31}$$

The apparent exchange current density on the anode side or the OER exchange current density can be calculated as follows (Bühre et al., 2024):

$$i_{0,a} = i_0^{\infty,\ OER} \exp\left(\frac{-E_A^{OER}}{RT}\right) \tag{32}$$

where E_A^{OER} and $i_0^{\infty,\ OER}$ represent the activation energy (21.7 kJ.mol^{-1}) and the exchange current density at the reference condition as temperature approaches infinity respectively, as reported in (Bühre et al., 2024). It is worth noting that this study relates the

Once the apparent exchange current density is determined, the specific exchange current density can be calculated using Eq. (31).

As shown in Eq. (31), for the sake of simplicity, this study evaluates the impact of Ir dissolution on the anodic overpotential by directly relating the Ir loading to the exchange current density. Consequently, a reduction in Ir loading due to its dissolution leads to a decrease in the exchange current density and, according to Eq. (56), an increase in the anodic overpotential. However, the present model does not explicitly account for degradation-induced changes in the ECSA, roughness factor, catalyst connectivity, porosity, or local current distribution. Capturing these effects would require a multiscale modeling framework that couples the micro-, meso-, and macroscale to resolve the morphology evolution arising from structural and textural changes within the anode catalyst layer. Therefore, the predicted contribution of anodic degradation should be interpreted in light of this modeling simplification. Although neglecting these morphology-related effects may influence the magnitude of the predicted anodic degradation, the direction and extent of the resulting bias cannot be established without a more detailed multiscale model.

2.3. Modelling the cathode chamber

On the cathode side of the PEM electrolysis unit, the reduction reaction, also known as the hydrogen evolution reaction (HER), occurs, as shown below:

$$2H^+ + 2e^- \rightarrow H_2 \tag{33}$$

Similar to the anode chamber, the accumulation of hydrogen in the cathode chamber is calculated by accounting for the hydrogen inlet and outlet flow rates, the hydrogen generation rate, and the hydrogen crossover to the anode side, using the following equation (Sorace, 2021):

$$\frac{dN_{ca,H_2}}{dt} = \dot{N}_{ca,H_2}^{in} - \dot{N}_{ca,H_2}^{out} + \dot{N}_{ca,H_2}^{gen} - \dot{N}_{ca,H_2}^{perm} \tag{34}$$

The hydrogen production rate at the cathode can be calculated using Faraday's law as follows:

$$\dot{N}_{ca,H_2}^{gen} = \frac{iA}{2F} \tag{35}$$

Similar to the oxygen crossover discussed in Section 2.1, hydrogen crossover is also influenced by both diffusion and electro-osmotic drag. However, unlike oxygen, hydrogen diffusion is opposed by electro-osmotic drag, as water transported by the drag moves from the anode to the cathode. Accordingly, hydrogen crossover in a PEM electrolysis unit is calculated using the following equations:

$$\dot{N}_{ca,H_2}^{perm} = \phi_{H_2}^{diff} - \phi_{H_2}^{drag} \tag{36}$$

$$\phi_{H_2}^{diff} = \frac{D_{H_2}.S_{H_2}.A_{cell}.P_{H_2,\ ca}}{t} \tag{37}$$

$$\phi_{H_2}^{drag} = \frac{iA}{F} n_d \frac{S_{H_2} P_{H_2,\ ca}}{c_{H_2O}} \tag{38}$$

where the solubility and diffusivity coefficients of hydrogen used in Eq. (37) are given as follows:

$$D_{H_2} = D_{H_2,0} \exp\left(\frac{-E_{A,H_2}}{RT}\right) \tag{39}$$

$$S_{H_2} = 0.55 \exp\left(A_{H_2} + \frac{B_{H_2}}{T} + C_{H_2} \ln\left(\frac{T}{100}\right)\right) \tag{40}$$

where E_{A,H_2} and $D_{H_2,0}$ represent the activation energy and the pre-exponential factor, respectively, while A_{H_2}, B_{H_2} and C_{H_2} are the constants. The values of the activation energy, pre-exponential factors, and

constants used to calculate the solubility and diffusivity of hydrogen and oxygen are provided in Table 2.

This study also considers and evaluates the agglomeration of platinum on the cathode side and its impact on the cathode overpotential. According to reference (Rakousky et al., 2016), no agglomeration of the anode catalyst layer was observed during long-term operation (1150 h) of the PEM electrolysis cell, and the crystal size on the anode side remained constant at 3.9 nm. Therefore, this study does not account for agglomeration of the anode catalyst material. The model used here to evaluate platinum agglomeration is based on the approach developed in reference (Liso et al., 2018). As the crystallite diameter of platinum increases due to agglomeration at an elevated operating temperature of 80 °C, the effective catalyst surface area decreases, resulting in a reduction of the roughness factor, which is defined as the ratio of the electrode active surface area to the membrane area and is given as follows (Liso et al., 2018):

$$\gamma_M = \phi_I m_M \frac{6}{\rho_M d_M} \tag{41}$$

where ϕ_I, m_M, ρ_M, and d_M represent the fraction of the metal catalyst available at the surface in contact with the ionomer, catalyst loading on the cathode side, density of the platinum catalyst, and crystallite diameter of the catalyst material, respectively. To model the growth of the platinum crystallite on the cathode side, the LSW equation was used to estimate the kinetics of particle growth under diffusion-limited conditions (Bucci et al., 2021):

$$r = \begin{cases} \sqrt[3]{r_0^3 + K_{LSW}^D t} \ if \ r < r_{critical} \\ r_{critical} \ \ if \ r_{critical} \leq r \end{cases} \tag{42}$$

where K_{LSW}^D and $r_{critical}$ represent the prefactor and critical radius of platinum particles, respectively. The prefactor can be calculated using the following equation:

$$K_{LSW}^D = \frac{8D\gamma_{Pt}\Omega^2 c^{eq}(V,\infty)}{9RT} \tag{43}$$

where D represents the effective diffusion coefficient of Pt^{2+}, with a value of 8×10^{-11} m^2/s according to reference (Ferreira et al., 2005), while γ_{Pt}, and $c^{eq}(V,\infty)$ represent the surface energy of platinum (2.78 J/m^2 according to reference (Bucci et al., 2021)), and the equilibrium concentration of platinum solution, respectively. The critical radius of platinum which refers to the maximum crystallite size, can be calculated as follows (Ostwald–Freundlich equation):

$$r_{critical} = \frac{2\gamma_{Pt} V_{Pt,atom}}{k_B T} \tag{44}$$

where k_B and $V_{Pt,atom}$ refer to Boltzmann constant and atomic volume of platinum, respectively. This study uses the data reported in reference (Siracusano et al., 2017) to estimate the growth rate of the platinum crystallites. According to this reference, after 1000 h of operation at a current density of 1 $A.cm^{-2}$, the crystallite size increased from 2.8 nm to 3.5 nm. The apparent exchange current density on the cathode side is then calculated as follows (Liso et al., 2018):

Table 2
Parameters used for calculating hydrogen diffusivity and solubility coefficients (Fahr et al., 2024).

Parameters	Values	Unit
$D_{H_2,0}$	4.9×10^{-6}	m^2/s
E_A	16,510	J/mol
A	−48.1611	-
B	5528.45	K
C	16.8893	-

$$i_{0,ca} = \gamma_M i_{0,ca}^* \tag{45}$$

The specific exchange current density on the cathode side can be calculated using an Arrhenius expression as follows (Liso et al., 2018):

$$i_{0,ca}^* = i_{0,ref} \exp\left(\frac{-E_a}{R}\left(\frac{1}{T} - \frac{1}{T_{ref}}\right)\right) \tag{46}$$

where $i_{0,ref}$ and E_a represent the reference exchange current density on the cathode side (0.001 $A.cm^{-2}$ (Liso et al., 2018)) and the activation energy (4300 J/mol (Liso et al., 2018)), respectively.

2.4. Membrane thinning

The transport of various species, including H_2O, H_2, and O_2, through the membrane via different mechanisms is discussed in detail in Sections 2.2 and 2.3 and will not be repeated here. Therefore, this section focuses solely on membrane degradation. The approach proposed by Chandesris et al. (2015) was adopted, in which ten reactions governing the production and consumption of various species, including H_2O_2, $H\dot{O}$, Fe^{2+}, Fe^{3+}, and $H\dot{O}\dot{O}$, are modeled (see Table 3). These reactions are used to calculate membrane thinning and to determine the membrane thickness over the course of cell operation. The rate of reactions listed in Table 3 are calculated as described in Chandesris et al. (2015) as follows:

$$v_i = \begin{cases} k_i c_{O_2} c_{H^+}^2 \ (i = 1) \\ k_i \prod_j c_j \ (1 < i \leq 10) \end{cases} \tag{47}$$

where i denotes the index of the reactions listed in Table 3, and c represents the concentration of the corresponding species in the reactions. The variation in species concentration over time was calculated using the following equation (Chandesris et al., 2015):

$$\frac{dc_j}{dt} = \sum_i sign(v_{ji})\delta_{ij})v_i + \frac{j_j^{in}}{e_{clC}} - \frac{j_j^{out}}{e_{clC}} \tag{48}$$

where v_{ji} and e_{clC} represent the stoichiometric coefficient of the jth species in the ith reaction and the thickness of the electrode, respectively, where δ_{ij} indicates whether the jth species participates in the ith reaction (1 if participates, 0 if not). In Eq. (48) j_j^{in} and j_j^{out}also represent the incoming molar flux and the convective transport of the jth species by water, respectively. The initial conditions for species concentrations employed in solving the system of ODEs in Eq. (48) and the initial thickness of the pristine membrane are provided in Table S1 of the Supplementary Materials. The convective transport of the jth species by water is calculated as follows:

$$j_j^{out} = v_{H_2O} c_j \tag{49}$$

Table 3
Summary of reactions involved in the membrane thinning of the PEM electrolysis cell (Chandesris et al., 2015).

1	$O_2 + 2H^+ + 2e^- \rightarrow H_2O_2$	$k_1 = k_{1o}^0 \exp\left(\frac{-A_{H_2O_2}}{RT}\right) \exp\left(\frac{-\alpha_{H_2O_2} F}{RT^0}\eta_{2e}\right)$
2	$H_2O_2 \rightarrow 2\,H\dot{O}$	$k_2 = 1.2 \times 10^{-7}$
3	$H_2O_2 + Fe^{2+} \rightarrow Fe^{3+} + H\dot{O} + HO^-$	$k_3 = 1.05 \times 10^8 \exp\left(\frac{-9640}{RT}\right)$
4	$H_2O_2 + Fe^{3+} \rightarrow Fe^{2+} + H\dot{O}\dot{O} + H^+$	$k_4 = 4 \times 10^{-5}$
5	$H\dot{O} + Fe^{2+} \rightarrow HO^- + Fe^{3+}$	$k_5 = 2.3 \times 10^8$
6	$H\dot{O} + H_2O_2 \rightarrow H\dot{O}\dot{O} + H_2O$	$k_6 = 2.7 \times 10^7$
7	$H\dot{O} + O_2 \rightarrow H\dot{O}\dot{O} + H_2O$	$k_7 = 1.2 \times 10^{10}$
8	$H\dot{O}\dot{O} + Fe^{3+} \rightarrow Fe^{2+} + O_2 + H^+$	$k_8 = 2 \times 10^4$
9	$H\dot{O}\dot{O} + Fe^{2+} + H^+ \rightarrow Fe^{3+} + H_2O_2$	$k_9 = 1.2 \times 10^6$
10	$H\dot{O} + R_f - CF_2 - COOH \rightarrow$ products	$k_{10} \leq 10^6$

where v_{H_2O} represents the velocity of water. It is worth noting that this study considers the impact of metallic ions originating from the corrosion of the stainless-steel pipes used for water supply to the system. As reported in Chandesris et al. (2015), approximately 70% of the generated ions are Fe^{2+}, with concentrations remaining on the order of a few ppm. Hence, this study incorporates a temperature-dependent source term for Fe^{2+}, which is expressed as follows (Chandesris et al., 2015):

$$S_{Fe^{2+}} = S\frac{T-290}{63} \tag{50}$$

It is worth noting that the concentration of these metallic ions has a significant impact on membrane degradation. Specifically, higher concentrations of dissolved metallic ions accelerate membrane thinning, leading to a deterioration in membrane performance because of the loss of sulfonic acid groups and reduction in its proton conductivity as described by Eq. (61). To compute the time-dependent concentration profiles of the five species, including H_2O_2, $H\dot{O}$, Fe^{2+}, Fe^{3+}, and $H\dot{O}O$ Eq. (48) was solved using MATLAB's ODE15s function, which is suitable for handling stiff, nonlinear, and coupled ordinary differential equations. In this study, the Fluoride Release Rate (FRR) is calculated using the following equation (Sorace, 2021):

$$FRR = 3600 v_{fluor} M_{fluor} t_m \tag{51}$$

In Eq. (51), v_{fluor} is calculated as 3.6 v_{10} according to reference (Chandesris et al., 2015). Finally, the membrane thinning rate (TR) is determined in unit of nm/hour using the following equation (Fouda-Onana et al., 2016):

$$TR = 10\frac{FRR}{0.82\rho} \tag{52}$$

2.5. Cell voltage

This section presents the calculation of the overpotentials that must be overcome in a PEM electrolysis cell to achieve hydrogen production. Based on the information from Sections 2.2–2.4, the anodic, cathodic, and ohmic overpotentials are determined, along with additional contributions such as open-circuit and concentration overpotentials relevant to modelling the PEM electrolysis unit. Accordingly, the cell voltage is determined by summing the individual overpotentials, as expressed by the following equation:

$$V_{cell} = V_{OC} + V_{act,ca} + V_{act,an} + V_{ohm} + V_{Con} \tag{53}$$

The open circuit overpotential, V_{OC}, shown in Eq. (53), represents the ideal cell voltage when no current is applied and no electrochemical losses are present. It is typically calculated as a function of the activities of hydrogen, oxygen, and water. To simplify the calculation and avoid the complexities associated with determining these activities, this study applies the ideal gas assumption to compute the open circuit overpotential using the following equation (Colbertaldo et al., 2017):

$$V_{OC} = E^0 + \frac{RT}{nF}\ln\left(\frac{P_{H_2}P_{O_2}^{0.5}}{a_{H_2O}}\right) \tag{54}$$

where a_{H_2O} represents the activity of water with value of 1 for liquid water. The reversible voltage can be expressed as a function of temperature using the following equation (Awasthi et al., 2011):

$$E^0 = 1.229 - 0.9 \times 10^{-3}(T-298) \tag{55}$$

The anodic overpotential is calculated using the following equation (Saidi et al., 2025):

$$V_{act,an} = \frac{RT}{F}sinh^{-1}\left(\frac{i}{2i_{0,a}}\right) \tag{56}$$

As discussed in Eq. (31), the anode exchange current density decreases slightly over time due to iridium dissolution and the associated reduction in iridium loading and thickness of the catalyst layer on the anode side, resulting in an increased anodic overpotential according to Eq. (56). It should be noted that this study does not model platinum dissolution. According to Dodwell et al. (2021), negligible platinum dissolution occurs only under open-circuit voltage conditions and drops to zero when current is applied to the cell.

Based on the apparent exchange current density and roughness factor determined in Section 2.3, the cathode overpotential can also be calculated as follows (Saidi et al., 2025):

$$V_{act,ca} = \frac{RT}{F}sinh^{-1}\left(\frac{i}{2i_{0,ca}}\right) \tag{57}$$

As shown in Table 3 oxygen crossover to the cathode side contributes to PEM electrolysis unit degradation through membrane thinning. In fact, membrane thinning significantly affects the performance of the PEM electrolysis cell. It not only increases H_2 and O_2 crossover resulting from a thinner membrane but also raises the ohmic overpotential by reducing the proton conductivity of the degraded membrane. In this study, the ohmic overpotentials of the electrodes are neglected, and only the membrane ohmic overpotential is considered, as described by the following equation (Sorace, 2021):

$$V_{ohm} = r_{mem} i \tag{58}$$

where r_{mem} represents the area-specific ohmic resistance which is defined as follows:

$$r_{mem} = \frac{t}{\sigma_{mem}} \tag{59}$$

The proton conductivity of a fresh membrane can be calculated as follows:

$$\sigma_{mem,fresh} = (0.005139\lambda - 0.00326)\exp\left(1268\left(\frac{1}{303} - \frac{1}{T}\right)\right) \tag{60}$$

It is worth noting that λ in Eq. (60) represents the water content of the membrane. This parameter is generally defined as the average ratio of the number of water molecules to the number of sulfonic acid groups in the membrane. The water content is a dimensionless quantity, with a value of zero for a dry membrane, and it can increase up to a maximum saturation value. Typically, λ varies between 14 and 21 (Escobar-Yonoff et al., 2021) for a fully hydrated membrane, depending on the membrane material and structure.

However, as noted above, membrane thinning and degradation decrease proton conductivity, thereby increasing the membrane ohmic resistance according to Eq. (59). The reduction in proton conductivity of the degraded membrane can be calculated as follows (Barbir, 2005):

$$\sigma_{mem} = \left(\frac{t}{t_0}\right)^2 \sigma_{mem,fresh} \tag{61}$$

The concentration overpotential arises from variations in the reactant concentrations at the electrode interfaces during the electrolysis process. This overpotential can be calculated using the following equation:

$$V_{Con} = \frac{RT}{\alpha_{an} zF}\ln\left(1 + \frac{i}{i_L}\right) \tag{62}$$

where i_L and α_{an} represent the diffusion-limited current density, with a value of 120 A.cm^{-2}, and the constant coefficient, with a value of 0.04, respectively, as reported in Lebbal and Lecœuche (2009).

Considering the degradation mechanisms discussed above, the energy efficiency of the PEM electrolysis unit can be estimated as follows (Yodwong et al., 2020):

$$\eta_{el} = \left(\frac{HHV\dot{N}_{H_2}}{v_{el}I_{el}}\right) \tag{63}$$

where I_{el} and v_{el} represent the applied current and cell voltage obtained by Eq. (53), respectively. The parameter set employed in this study for modeling the PEM electrolysis cell, encompassing the electrochemical, thermodynamic, and degradation sub-models, is presented in Table S2. The methodology employed to model the various degradation mechanisms is also detailed in the Supplementary Materials.

3. Results and discussion

This section presents the results of the model developed to evaluate the main degradation mechanisms described in Section 2. Fig. 4 shows the polarization curves of a fresh cell and a degraded cell operated for 20,000 h under baseline conditions (80 °C temperature, 1 bar pressure and 1 A.cm^{-2} current density), measured at temperatures ranging from 60 °C to 90 °C. As observed, operating at lower temperatures increases the cell voltage of the pristine cell, leading to higher power consumption and reduced energy efficiency at BOL. However, operation at elevated temperatures (e.g., 90 °C) accelerates degradation, resulting in a higher cell voltage after 20,000 h of operation due to increased membrane thinning rates, the formation of hot spots, and catalyst layer agglomeration at the cathode. Therefore, in this study, cell performance is evaluated at 80 °C, which represents a balance between efficiency and durability. It is worth noting that at low current densities, activation overpotentials dominate due to slow reaction kinetics. At intermediate to high current densities, ohmic overpotentials become the primary source of voltage losses, as illustrated in Fig. 4. As can be observed, since the degraded cell exhibits higher ohmic overpotentials, a steeper voltage increase with current density is observed after 20,000 h of operation.

Fig. 5 also compares the change in membrane thickness, expressed as a percentage of the fresh membrane thickness, for a PEM electrolysis cell after 20,000 h of operation with the results reported by Chandesris et al. (2015) for a cell operated at a current density of 1 A.cm^{-2} and a temperature of 80 °C. The results obtained from our model are consistent with those of Chandesris et al. (2015) with RMSE of 4.13%. To further verify the model developed in this study and evaluate its performance, the operating conditions reported in reference (Su et al., 2024) were adopted. The model results were then compared with the experimental data presented in reference (Su et al., 2024). As shown in Fig. 6, the model predictions are in good agreement with the experimental data with a maximum relative error of 0.83%, demonstrating that the model accurately predicts the performance of the PEM electrolysis cell over 600 h of operation at 80 °C and a current density of 1 and 2 A.cm^{-2}. Fig. 7 also compares the voltage degradation predicted by the model developed in this study with the experimental results reported in Padgett et al. (2025) under identical operating conditions, namely current densities of 1 A cm^{-2} and 2 A cm^{-2}, atmospheric pressure and 80 °C temperature over an extended operating period of 4000 h. As shown in the figure, the model predictions exhibit good agreement with the experimental data reported in (Padgett et al., 2025) with a maximum relative error of 1.52%, demonstrating the capability of the proposed model to accurately capture the long-term voltage degradation behavior of the CCM in the PEM electrolysis cell. It is worth noting that although this study evaluates the voltage degradation of a PEM electrolysis cell over extended operating periods (e.g., until the EOL and after 20,000 h of operation), these long-term predictions, particularly under dynamic LC and idle operation, should be regarded as extrapolations. This is because the model has been validated only up to 4000 h of operation, owing to the limited availability of long-term experimental degradation data in the literature.

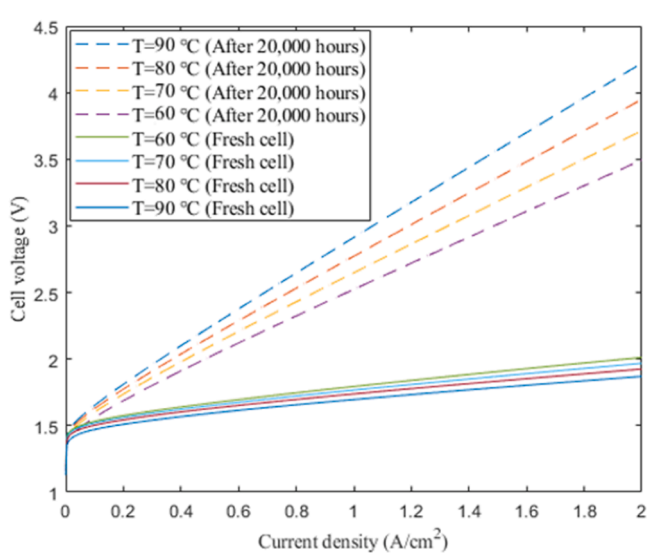

Fig. 4. Polarization of fresh cell and degraded cell after operating for 20,000 h under baseline operating conditions.

This section examines the degradation of the PEM electrolysis cell under the baseline operating conditions as well as under variable operating conditions. Specifically, it assesses the impact of cycling the current density between 1 and 2 A.cm^{-2} every 6 h, together with variations in temperature, pressure, operating current density and frequent idle operation, on the degradation of cell voltage and energy efficiency.

3.1. Operating the cell under constant load

Fig. 8 shows the reaction rate responsible for membrane thinning (reaction 10 in Table 3), commonly referred to as hydroxyl-radical attack. As illustrated, membrane thinning driven by hydroxyl-radical attack leads to a substantial reduction in proton conductivity over time because of the loss of sulfonic acid groups (Xing et al., 2021). Consequently, as expressed in Eqs. (58) and 59, the ohmic resistance and therefore the ohmic overpotential increase significantly as the membrane's proton conductivity decreases.

Fig. 9 shows how iridium loading and the thickness of the catalyst layer change on the anode side over time when the cell operates at a current density of 1 A.cm^{-2} and a temperature of 80 °C. As observed, both iridium loading and thickness of the catalyst on the anode side decrease slightly over 20,000 h of operation. This minimal degradation is primarily attributed to the very large S_{number}, which leads to a very low iridium dissolution rate according to Eq. (26). As a result, the catalyst layer thickness decreases by only 5.74% over the entire 20,000-hour period.

Fig. 10 illustrates the variation of the roughness factor as the crystallite diameter of platinum catalyst particles on the cathode side increases over 20,000 h of operation. As shown, growing the crystallite diameter from 2.8 nm to 7.852 nm leads to 64.33% reduction in the roughness factor, and thereby the ECSA. Consequently, the apparent exchange current density decreases from 0.2948 A.cm^{-2} to 0.1051 A.cm^{-2}, which results in increasing the cathodic overpotential by 74.25%.

Fig. 11 shows the variation of different overpotentials, namely ohmic, open-circuit, concentration, anodic, and cathodic, over 20,000 h of operation at a constant load and current density of 1 A.cm^{-2}, and temperature of 80 °C. Although this study evaluated the performance of the modeled cell over 20,000 h of operation, the cell reaches its end of life (EOL) earlier. According to Sparber et al. (2013), a PEM electrolysis system is considered to have reached EOL when the power loss exceeds 20% of its nominal power input. Therefore, as shown in Fig. 11, the electrolysis cell reaches EOL after approximately 13,000 h of operation. It should be noted that, in the figures presented in Section 3, the EOL, indicated by the vertical dashed lines, corresponds to the end of life of the cell under the baseline operating conditions (T = 80 °C, P = 1 bar with constant current density of i = 1 A.cm^{-2}), unless otherwise specified. As observed, the variations in concentration, anodic, and open circuit overpotentials are negligible throughout the operation period. In contrast, the increase in cathodic overpotential, caused by catalyst

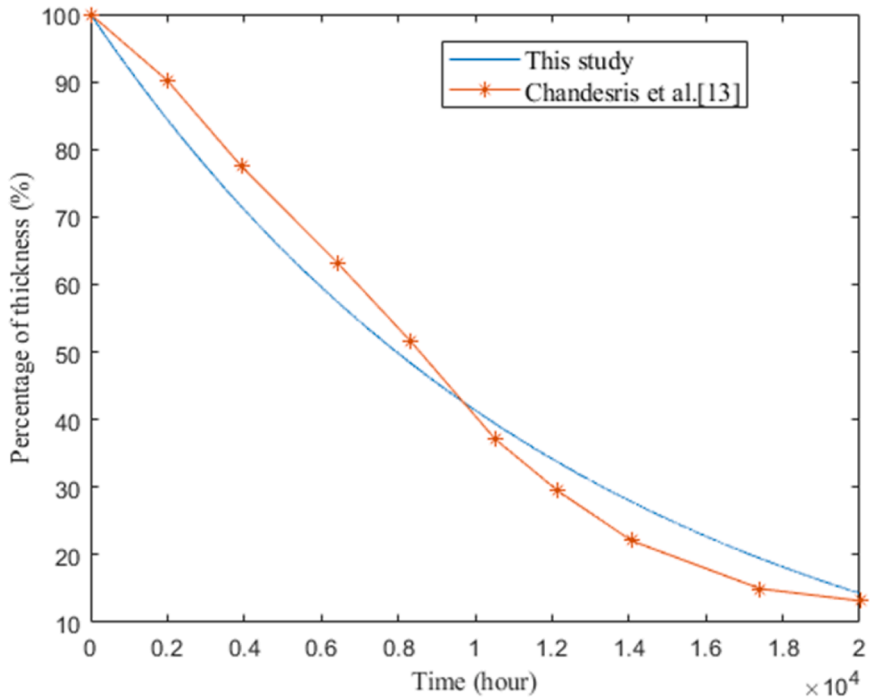

Fig. 5. Validation of model results for membrane thinning (Chandesris et al., 2015).

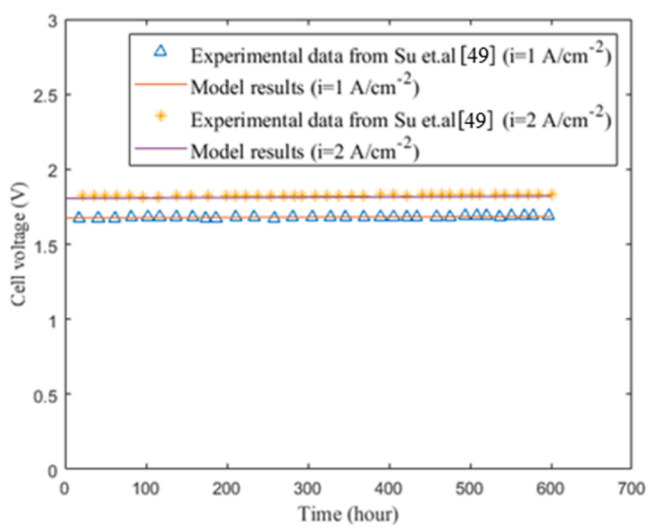

Fig. 6. Validation of model performance against experimental data for predicting voltage degradation in a PEM electrolysis cell over 600 h of operation (Su et al., 2024).

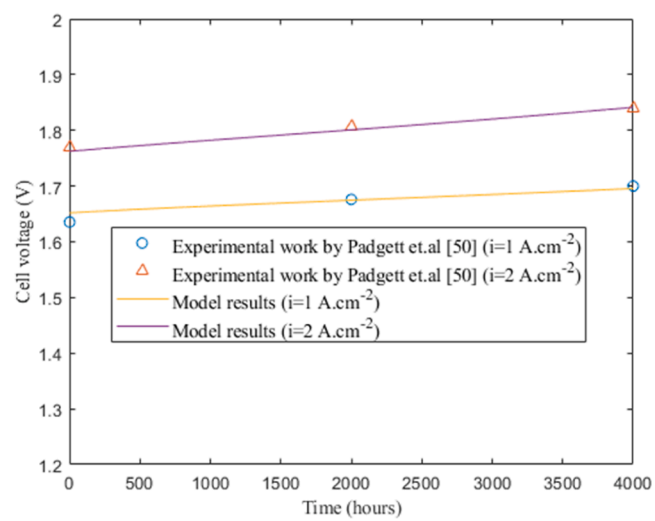

Fig. 7. Validation of the model predictions against experimental data for voltage degradation in a PEM electrolysis over an extended operating period of 4000 h (Padgett et al., 2025).

agglomeration on the cathode side, and particularly the increase in ohmic overpotential due to membrane thinning, are more pronounced. Specifically, the ohmic overpotential increases from 0.1433 V at the BOL to 0.4662 V at the EOL, reaching 1.0228 V after 20,000 h of operation. The cathodic overpotential also increases more gradually, from 0.0398 V at BOL to 0.0649 V at EOL and 0.0689 V after 20,000 h of operation. These effects collectively result in a 52.34% increase in cell voltage over 20,000 h of operation.

Fig. 12 illustrates the time evolution of hydrogen and oxygen crossover resulting from membrane thinning shown in Fig. 5, together with the variation of hydrogen-to-oxygen (HTO) diffusion over time. As can be seen, hydrogen crossover is more pronounced than oxygen crossover, which is consistent with the findings presented by Fahr et al. (2024). It is worth noting that the hydrogen and oxygen crossovers shown in Fig. 12 are closely linked to membrane thinning and its degradation. As the membrane becomes thinner, the crossover rates of both gases increase. In particular, the higher oxygen concentration on the cathode side accelerates membrane thinning due to its increased crossover rate, thereby further contributing to the overall membrane degradation. Hence, both hydrogen and oxygen crossovers increase with time because the thinner membrane provides less resistance to gas separation between the cathode and anode sides. As discussed in Sections 2.2 and 2.3, diffusion is the primary mechanism governing hydrogen and oxygen crossover, and it is influenced by the concentration or partial pressure of hydrogen and oxygen on the cathode and anode sides, respectively. Since hydrogen has a higher diffusion

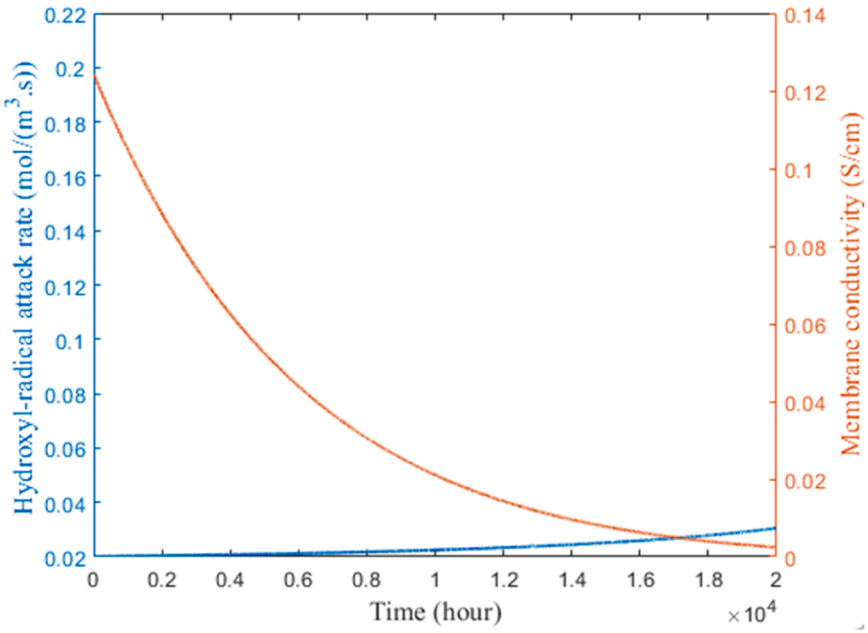

Fig. 8. Evolution of hydroxyl-radical attack rate and membrane conductivity over time.

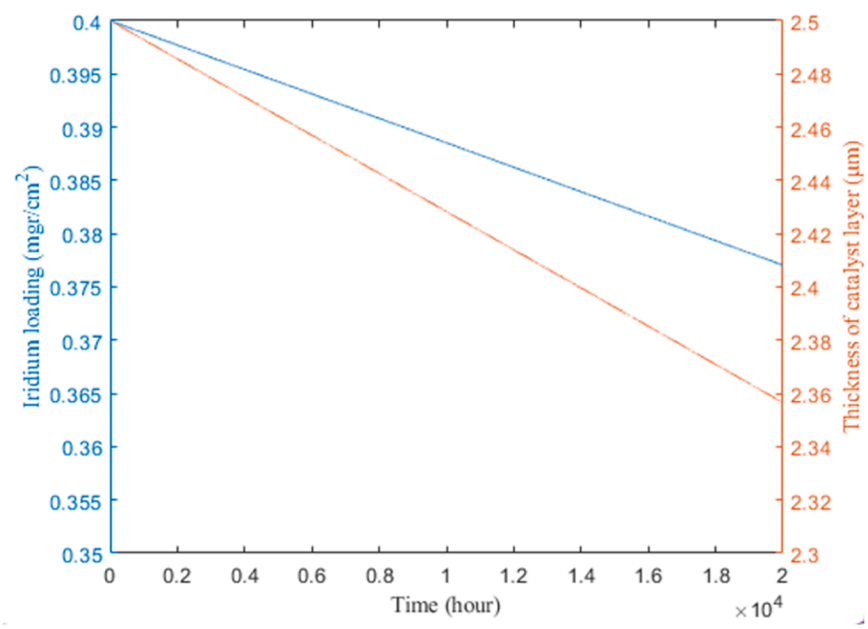

Fig. 9. Variation of the iridium loading and thickness of catalyst layer on the anode side over the time.

coefficient than oxygen, its crossover rate is higher, as shown in Fig. 12. Furthermore, the figure indicates that the HTO diffusion also increases over time. In fact, the oxygen-to-hydrogen (OTH) diffusion is inherently low and thereby, typically does not pose safety concerns. On the other hand, HTO is a critical parameter, and it is essential to keep it low to avoid explosion risks. Accordingly, the HTO must remain below 2%, as specified in de Groot et al. (2022). As shown in Fig. 12, although the HTO reaches 3.15% after 20,000 h of operation, it does not exceed 1.43% at the EOL, thereby ensuring safe operation of the electrolysis cell.

Fig. 13 illustrates the variation of cell energy efficiency over time during hydrogen production. The fresh PEM electrolysis cell exhibits a high initial energy efficiency of 85.04% at the start of operation for green hydrogen generation. However, the cell performance and consequently its energy efficiency decline significantly over time due to degradation mechanisms such as platinum catalyst crystallite agglomeration on the cathode side, iridium dissolution on the anode side, and, most critically, membrane thinning. The reduction in output hydrogen flow rate on the cathode side, caused by increased hydrogen crossover through the membrane thinning, combined with the rise in power consumption due to overall cell degradation, leads to a 30 % decrease in cell energy efficiency over 20,000 h of operation.

Fig. 14 illustrates the contributions of different overpotentials at the BOL, EOL, and after 20,000 h of operation of the PEM electrolysis cell. At BOL, the ohmic overpotential is relatively small. However, it increases by approximately a factor of 3.2 at EOL and by a factor of 7 after 20,000 h of operation, primarily due to membrane thinning. In addition, as discussed in Fig. 11, agglomeration of platinum crystallites on the

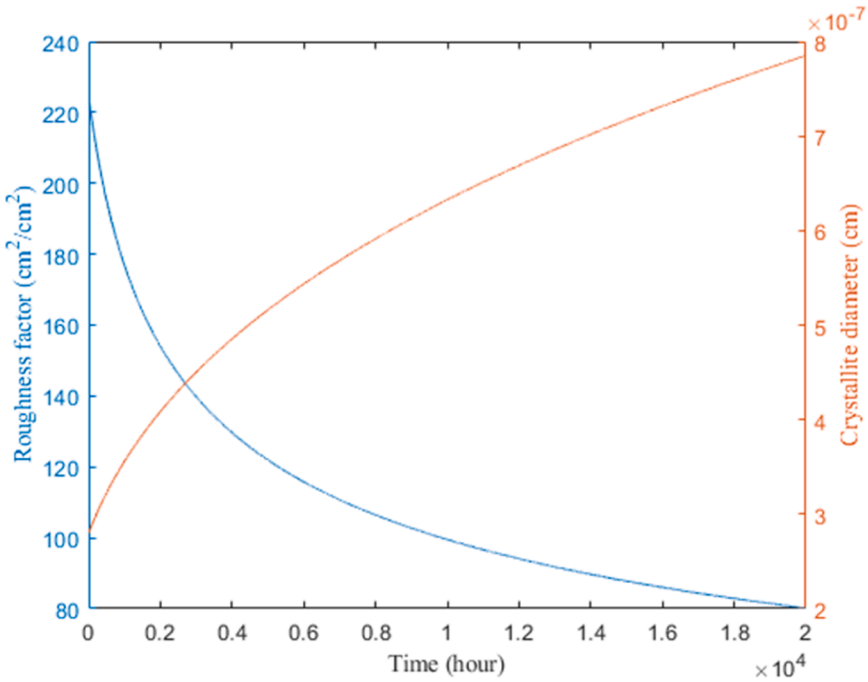

Fig. 10. Variation of roughness factor and crystallite size of the cathode electrode over time.

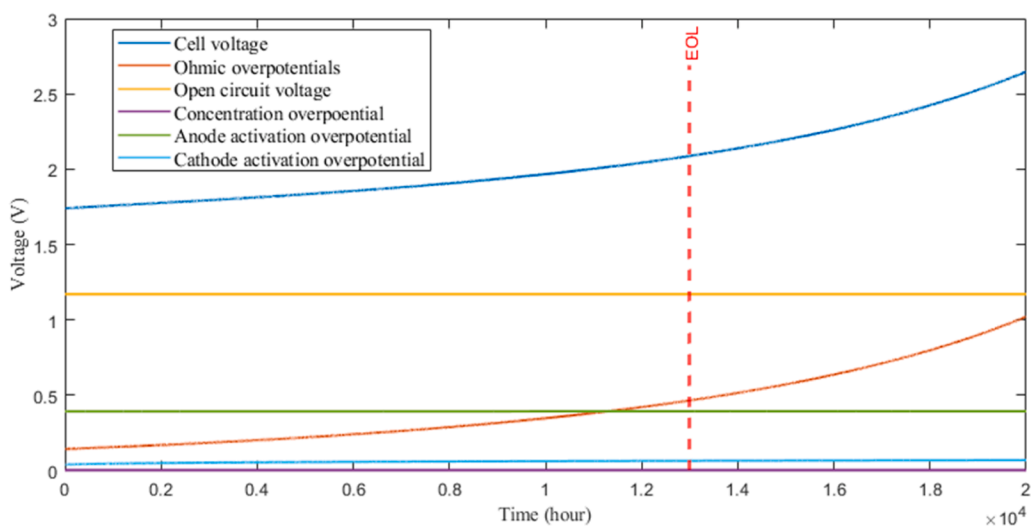

Fig. 11. Variation of cell voltage and overpotentials over 20,000 h of operation at a constant load and current density of 1 A.cm^{-2}, and temperature of 80 °C.

cathode electrode becomes more pronounced over time, leading to higher cathodic overpotentials at EOL and after 20,000 h of operation compared with BOL as shown in Fig. 14. Consequently, as shown in the figure, the overall cell voltage rises from 1.739 V at BOL to 2.089 V at EOL, and further to 2.65 V after 20,000 h of operation.

3.2. *Impact of the current density on performance and degradation of the cell*

Fig. 15 illustrates the impact of operating current density on the cell voltage and its degradation over time, comparing operation at current densities of 1 A.cm^{-2} and 2 A.cm^{-2} over a temperature of 80 °C and a pressure of 1 bar. As shown, increasing the current density leads to higher overpotentials particularly ohmic, cathodic, and anodic contributions and thereby higher cell voltage. Specifically, increasing the current density from 1 A.cm^{-2} to 2 A.cm^{-2} doubles the ohmic overpotential, as indicated by Eq. (58). In addition, as described in Eqs. (56) and 57, both the anodic and cathodic overpotentials also increase as the current density rises from 1 A.cm^{-2} to 2 A.cm^{-2}. Hence, operating the cell at a current density of 2 A.cm^{-2} instead of 1 A.cm^{-2} results in a 10.75% increase in cell voltage at the BOL. Furthermore, operation at higher current densities leads to a higher iridium dissolution rate as shown by Eq. (26), which in turn results in a thinner anode electrode and thereby, a higher anodic overpotential. Hence, as shown in the figure, the PEM electrolysis cell exhibits a higher degradation rate over the time when operated at 2 A.cm^{-2}, primarily due to increased anodic and cathodic degradations. Consequently, as shown in Fig. 15, increasing the current density of the PEM electrolysis cell from 1 A.cm^{-2} to 2 A.cm^{-2} leads to an accelerated degradation rate, resulting in a 27% reduction in the lifetime and a 1.78-fold increase in voltage degradation after 20,000 h of operation. Although operating the PEM electrolysis unit at higher current densities enhances hydrogen production and reduces the initial

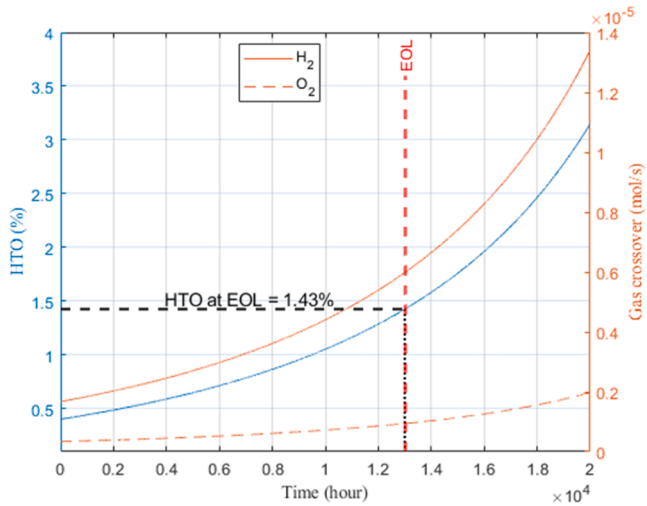

Fig. 12. Gas crossover and HTO after 20,000 h of operation.

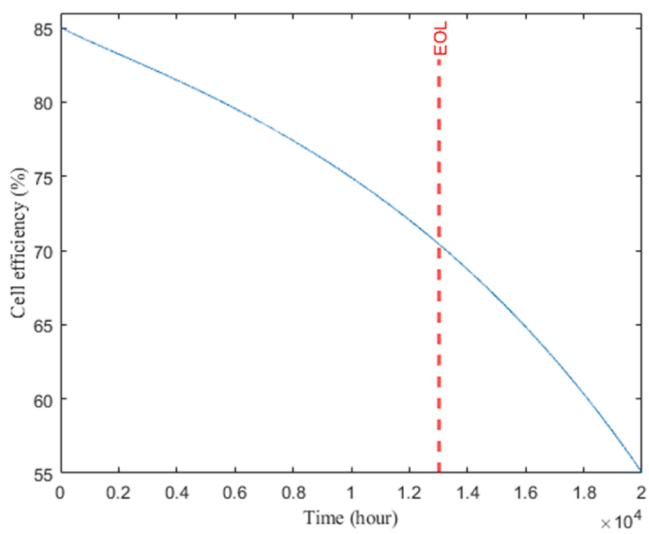

Fig. 13. Variation of cell efficiency when operating under constant load.

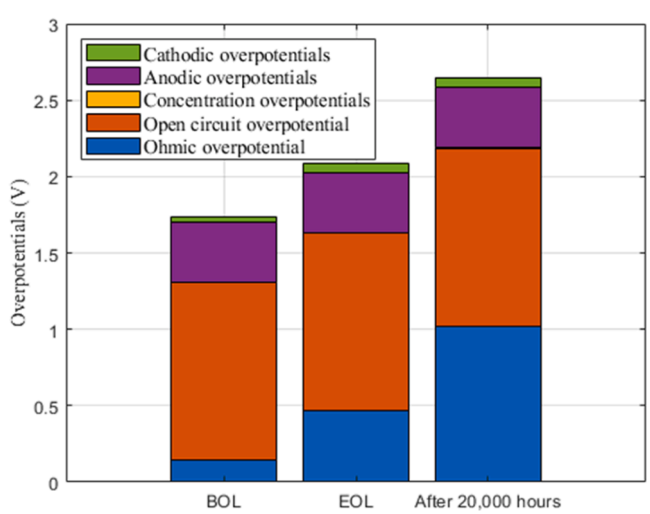

Fig. 14. Contribution of the overpotentials of the cell at the beginning and end of life of the cell.

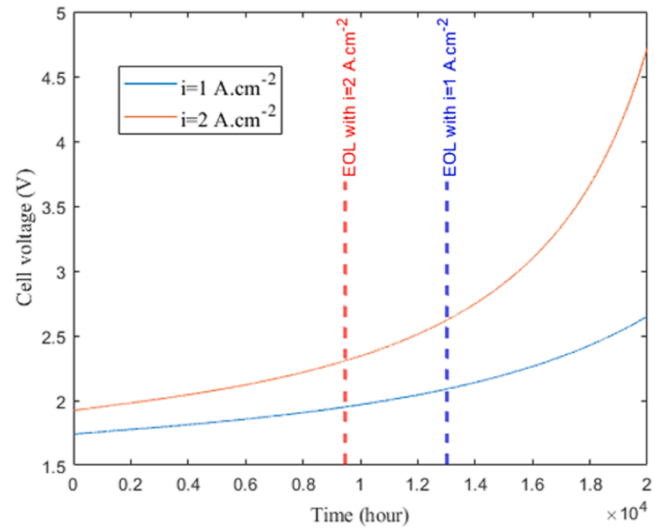

Fig. 15. Variation of cell voltage over time when increasing the current density from 1 Acm^{-2} to 2 Acm^{-2}.

capital costs, it also leads to accelerated degradation and higher electricity costs at the EOL.

Fig. 16 illustrates the impact of current density on cell efficiency during operation at current densities ranging from 1 $A.cm^{-2}$ to 2 $A.cm^{-2}$ over 20,000 h. As shown, operating the cell at lower current density of 1 $A.cm^{-2}$ results in higher energy efficiency, particularly at EOL and after 20,000 h of operation. Although operating at 2 $A.cm^{-2}$ doubles the hydrogen production rate compared to 1 $A.cm^{-2}$, the increased power consumption, caused by higher overpotentials (as discussed in Fig. 15) and greater applied current, reduces the overall cell energy efficiency, as depicted in Fig. 16. Initially, the fresh cell exhibits 8.16% higher efficiency at 1 $A.cm^{-2}$. Over time, degradation becomes more pronounced at higher current densities (as also shown in Fig. 15), leading to efficiency losses of 30% at 1 $A.cm^{-2}$ compared with 37.34% at 2 $A.cm^{-2}$ after 20,000 h of operation.

3.3. Impact of load cycling on performance and degradation of the cell

This section examines the impact of LC on the performance and

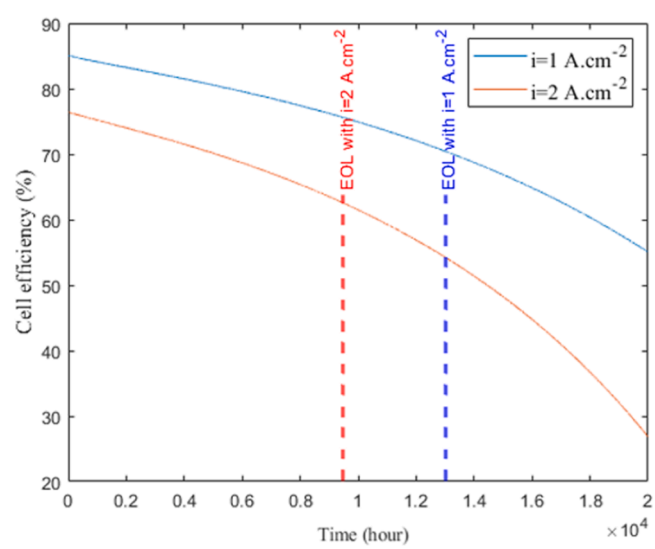

Fig. 16. Variation of cell efficiency when operating the cell at current density of 1 $A.cm^{-2}$ and 2 $A.cm^{-2}$ for 20,000 h of operation.

degradation of the PEM electrolysis cell. In this study, the current density is cycled between 1 A.cm^{-2} and 2 A.cm^{-2} every six hours. According to reference (Rakousky et al., 2017), the degradation rate under these conditions caused by LC is estimated at 65 μVhr^{-1}. Fig. 17 illustrates the effect of current density cycling over a 120-hour (five-day) period. It is worth noting that this period was chosen to maintain the clarity of the plots shown in Figs. 17 and 18. As shown, LC causes the cell voltage to increase from 1.739 V to 1.7466 V over the five days of operation.

Fig. 18 also illustrates the impact of LC on the energy efficiency of the PEM electrolysis cell. Consistent with the results shown in Fig. 16, the cell exhibits higher efficiency when operating at a current density of 1 A.cm^{-2}, primarily because the ohmic overpotentials are significantly lower when operating the cell at lower currents. Furthermore, as shown in this figure, cycling the current density between 1 A.cm^{-2} and 2 A.cm^{-2} every six hours for five consecutive days results in a 0.358% reduction in cell efficiency.

Fig. 19 compares the voltage degradation due to LC predicted in this study with the experimental data reported in Rakousky et al. (2017). The figure illustrates the increase in cell voltage during operation at a current density of 2 A.cm^{-2}, with the current density cycled between 1 A.cm^{-2} and A.cm^{-2} every six hours. Although a slight deviation exists between the pristine cell voltages reported in Rakousky et al. (2017) and calculated in this study at a current density of 2 A.cm^{-2}, which can be attributed to differences in cell characteristics, the voltage increase after 1000 h of operation is in good agreement. The relative error between the predicted and experimental voltage rise is only 3.73%.

3.4. The impact of idle operation on the degradation of the cell

When evaluating the degradation of CCM within the PEM electrolysis cell powered exclusively by renewable energy sources, it is essential to assess the impact of idle operation during the periods when renewable power is unavailable. Therefore, this section investigates the effects of idle operation and hot start-up events on the degradation of the CCM in a PEM electrolysis cell. Specifically, the analysis focuses on the dissolution of the iridium catalyst in the anode electrode and membrane thinning. It is worth noting that the results presented in this section are valid only for the specific operating conditions considered in this study, including an asymmetric pressure configuration (16 bar at the cathode and atmospheric pressure at the anode), an operating temperature of 80 °C, and an operation cycle consisting of 10 min of idle operation every 20 min, during which the current density varies between 1 A.cm^{-2} and zero.

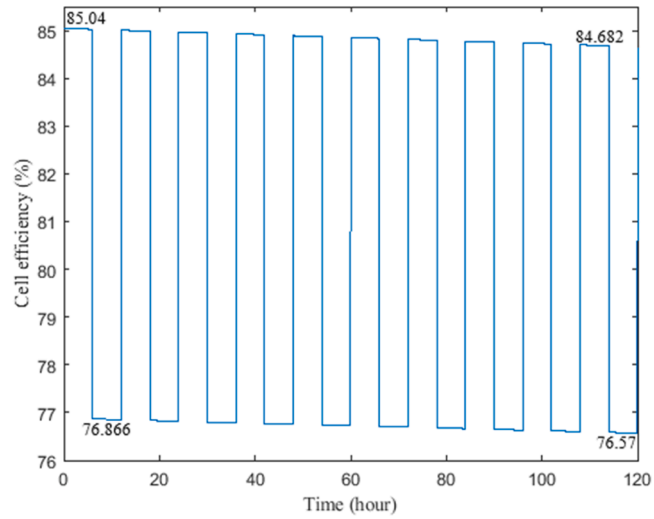

Fig. 18. The impact of LC on the cell efficiency of a PEM electrolysis unit.

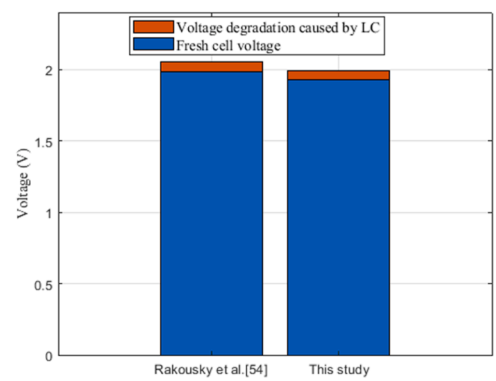

Fig. 19. Validation of the model performance for evaluating the voltage degradation caused by LC.

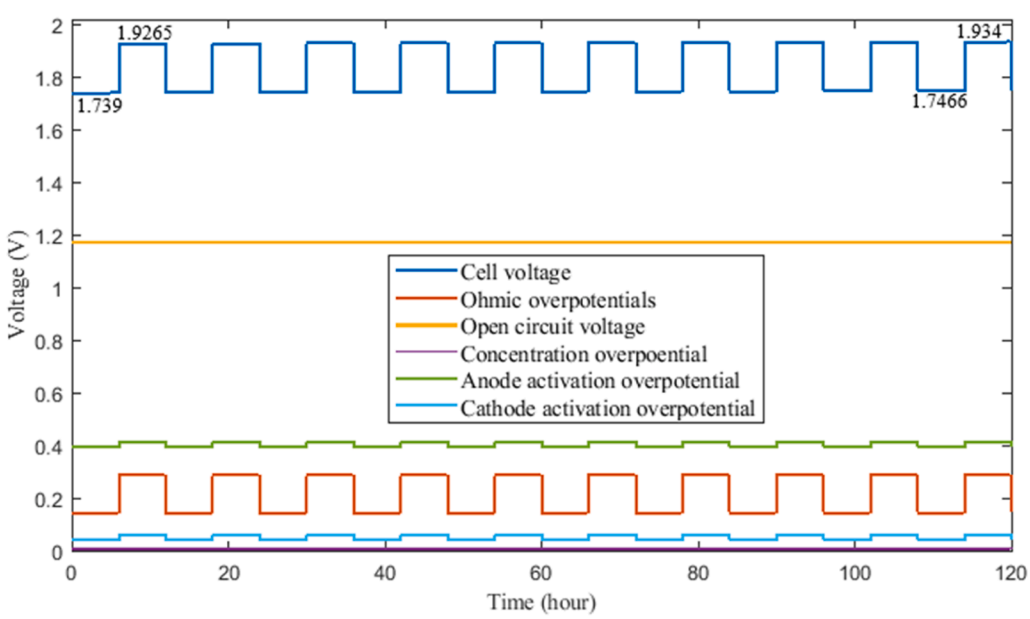

Fig. 17. The impact of LC on the cell voltage and its degradation.

Therefore, the predicted degradation behavior discussed in this section may vary when these operating parameters are changed. Consequently, the results reported in this section may not be applicable to other intermittent operating scenarios of PEM electrolysis cells.

According to Milosevic et al. (2026) the stability number used in Eq. (26) decreases when the cell undergoes idle operation followed by hot start-up after shutdown. As a result, Eq. (26) predicts an increase in the iridium dissolution rate. Based on the data reported in Milosevic et al. (2026), a PEM electrolysis cell subjected to an operating cycle consisting of 10 min of idle operation every 20 min, during which the current density decreases from 1 A.cm^{-2} to zero, exhibits a time-dependent stability number. Since this operating profile is similar to the one considered in the present study, the stability number is described by the following equation rather than by Eq. (25), which assumes operation at a constant current density of 1 A.cm^{-2}.

$$S_{number} = 6 \times 10^6 ln(t) + 428960 \tag{64}$$

where t represents the operating time in seconds. Consequently, using this time-dependent stability number given in Eq. (64) to calculate the iridium dissolution rate results in higher dissolution rates compared with the case of constant-current operation. This accelerated iridium loss leads to a faster increase in the anodic overpotential during the cell operation.

The evolution of the anodic overpotential resulting from anode degradation caused by iridium dissolution is compared in Fig. 20 for two operating scenarios: continuous operation at a constant current density of 1 A.cm^{-2} and operation with frequent idle periods. As shown in Fig. 20, the idle operation associated with the intermittent nature of renewable energy sources significantly increases the anodic overpotential, thereby accelerating the performance degradation of the CCM. It is primarily driven by redox processes occurring within the anode catalyst layer, which lead to the formation of IrO_x species. These species exhibit higher activity but also show increased dissolution rates under OER conditions, as highlighted in Milosevic et al. (2026). Additionally, reference (Milosevic et al., 2026) also highlights that the performance degradation associated with idle operation becomes more pronounced when the cell is subjected to frequent idle cycling over longer periods. This observation is consistent with the results presented in Fig. 20.

Idle operation of a PEM electrolysis unit during periods when renewable power is unavailable can lead to accelerated membrane thinning, particularly under asymmetric pressure conditions. In such configurations, as discussed in Kuhnert et al. (2023) and Minnah and Pope (2026), hydrogen crossover increases during idle operation due to the high cathode pressure (16 bar) combined with atmospheric pressure at the anode. This effect is primarily attributed to hydrogen accumulation on the cathode side and the maintenance of pressure even when the cell is not operating. Although the present study considers a PEM electrolysis unit operating under symmetric pressure conditions (atmospheric pressure on both anode and cathode sides), an asymmetric pressure configuration (16 bar at the cathode and atmospheric pressure at the anode) is introduced in this section to capture the impact of idle operation on membrane thinning. As discussed in Kuhnert et al. (2023), under such conditions, high hydrogen crossover can also lead to the formation of radicals on the anode side. As a result, the membrane is subjected to radical attack from both the cathode and anode sides. The mechanisms of membrane thinning on the cathode side are discussed in Section 2.4, while anode-side radical formation and attack mechanisms are thoroughly described in Kuhnert et al. (2023) and are not repeated here. For the sake of simplicity, a correction factor is introduced in this study to account for the increased radical formation on both sides of the membrane, thereby enabling a faster membrane thinning rate under idle operation conditions. This correction factor is calibrated to reproduce the membrane thinning behavior reported in Minnah and Pope (2026) under identical operating conditions (80 °C and asymmetric pressure) with frequent idle operation. Hence, in Minnah and Pope (2026), a membrane thickness reduction of 96.2 μm after 8000 h of operation with frequent idle cycling is reported, whereas the present model predicts a reduction of 89.7 μm under constant-load operation, corresponding to a 50.42% decrease from the initial thickness of 178 μm, as shown in Fig. 5. To align the model with the reported degradation behavior, a correction factor of 1.12 is therefore applied to $H\dot{O}$ radical formation rate. Fig. 21 compares the evolution of membrane thickness and ohmic overpotential under constant-load operation and under conditions involving frequent idle operation.

Fig. 22 also compares voltage degradation and the time required to reach the EOL under constant-load operation and operation with frequent idle periods. As shown, the PEM electrolysis cell operating under a constant load exhibits a lower degradation rate and reaches EOL later. In contrast, frequent idle operation accelerates degradation, causing the cell to reach EOL after 11,405 h compared to 13,000 h under constant-load conditions. Furthermore, the figure shows that the cell operating with frequent idle periods reaches a higher cell voltage after 20,000 h of operation (2.99 V), reflecting the increased degradation rate associated with idle operation. Specifically, the results presented in Fig. 22 are valid only for the operating conditions considered in this study, including an asymmetric pressure configuration (16 bar at the cathode and atmospheric pressure at the anode), an operating temperature of 80 °C, and an operation cycle consisting of 10 min of idle operation every 20 min, during which the current density varies between 1 A.cm^{-2} and zero. Therefore, these results may not be applicable to other operating conditions or intermittent operation scenarios. This limitation arises because the results shown in this section are obtained based on the applied correction factor and the empirical correlation for S_{number} provided in Eq. (64), which may not remain valid when different operating conditions and idle operation strategies are considered. Fig. 23 compares the contributions of different overpotentials, particularly the anodic and ohmic overpotentials associated with iridium dissolution and membrane thinning, respectively, to the voltage degradation of the PEM electrolysis cell under constant-load operation (marked as C in the figure) and intermittent operation with frequent idle periods (marked as I in the figure), as discussed above. The comparison is performed at BOL, EOL, and after 20,000 h of operation. As shown in the figure, when the cell is operated with frequent idle periods, it reaches the EOL earlier due to the accelerated increase in iridium dissolution and membrane thinning. Consequently, at the EOL (after 11,405 h), the membrane remains slightly thicker, resulting in slightly lower ohmic overpotentials compared with constant-load operation which reaches

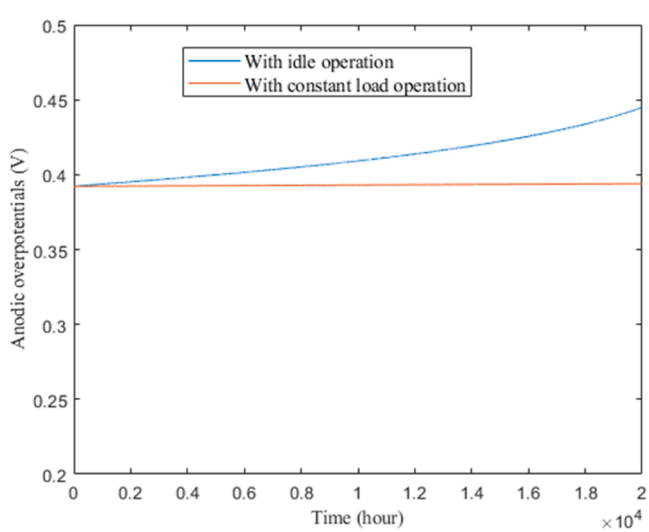

Fig. 20. Comparison of degradation of anodic overpotentials when operating the cell under constant current and frequent idle operation.

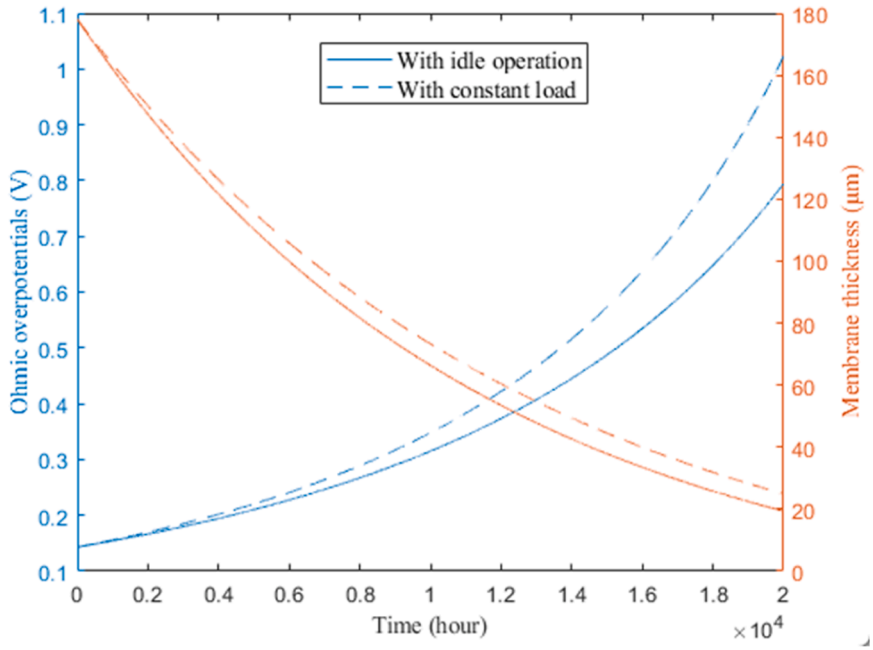

Fig. 21. Comparison of ohmic overpotentials and Membrane thinning when operating the PEM electrolysis cell with constant load and frequent idle operation.

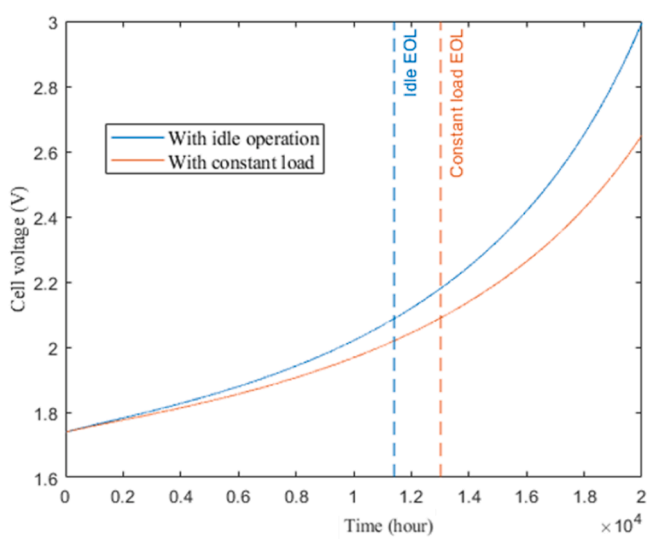

Fig. 22. Comparison of cell voltage degradation and EOL between constant load operation and frequent idle operation.

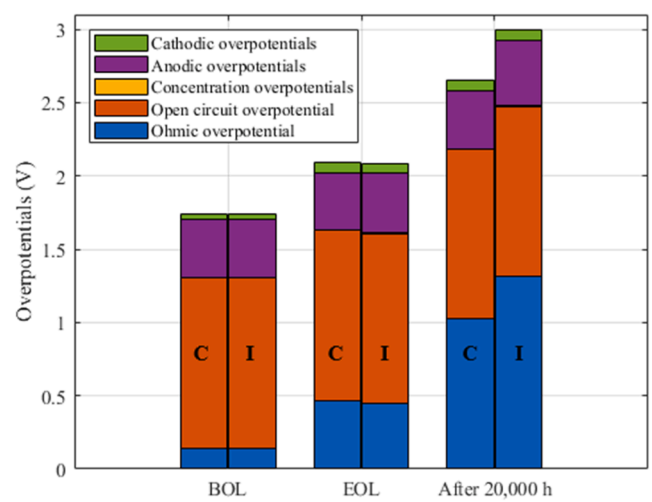

Fig. 23. Comparison of different overpotential contributions at BOL, EOL, and after 20,000 h of operation under constant-load operation (marked as C) and intermittent operation with frequent idle periods (marked as I).

EOL after 13,000 h. However, after 20,000 h of operation, the cell operated with frequent idle periods exhibits higher anodic and ohmic overpotentials, with the ohmic overpotential increasing by 28.5% compared with constant-load operation.

3.5. Impact of temperature on performance and degradation of the cell

Fig. 24 illustrates the effect of cell temperature on its performance and degradation. As shown, operating the cell at higher temperatures enhances the performance by reducing overpotentials. In particular, operating the PEM electrolysis unit at 80 °C leads to lower overpotentials at BOL. Hence, as shown in the figure, the cell efficiency is higher at 80 °C at BOL. However, the figure also shows that operation at this elevated temperature results in accelerated degradation, leading to a significantly higher cell voltage and also lower energy efficiency after 20,000 h of operation. Specifically, at EOL and after 20,000 h of operation, the cell's energy efficiency is 2.13% and 8.18% lower, respectively, when operated at 80 °C compared to 70 °C.

3.6. Impact of pressure on performance and degradation of the cell

This section also discusses the impact of operating pressure on cell performance and its degradation. Accordingly, Fig. 25 illustrates how the degradation of the cell voltage during operation is affected by operating pressure. As shown, operating the cell at higher pressure leads to increased cell voltage, primarily due to increased open circuit voltage due to higher partial pressures of oxygen and hydrogen as discussed in Eq. (54) and also increased oxygen crossover and accelerated membrane thinning caused by higher rates of hydrogen peroxide generation (see Table 3). The combination of membrane thinning due to degradation and the elevated operating pressure leads to significantly higher oxygen

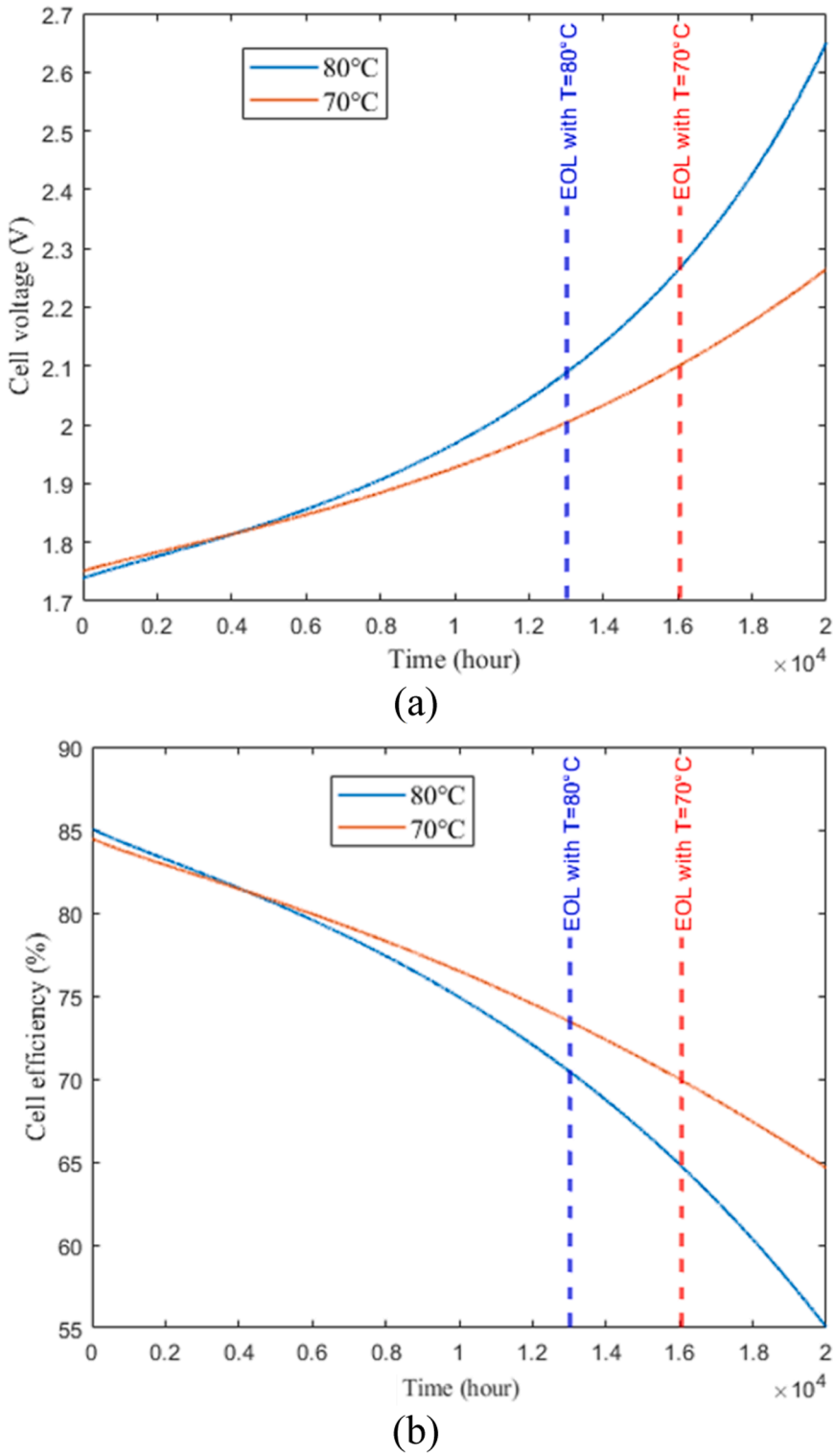

Fig. 24. The impact of operating cell temperature on (a) cell voltage (b) energy efficiency after 20,000 h of operation.

crossover, which further accelerates membrane degradation. Consequently, after 20,000 h of operation, the cell overpotentials are 4.16% higher when operating at an elevated pressure of 5 bars compared to 1 bar, whereas at BOL, the cell voltage was 3% higher under the same pressure conditions. It is worth noting that, for clarity, only the EOL at 1 bar is shown in Fig. 25. Although operation at higher pressure may slightly increase degradation, it does not significantly affect EOL. According to Fig. 25, the effect of operating pressure on cell efficiency is more pronounced when compared with its effect on cell voltage at an operating current density of 1 A.cm^{-2} and a temperature of 80 °C. In this case, both higher overpotentials and increased hydrogen crossover contribute to a more noticeable reduction in cell efficiency. Specifically, increasing the operating pressure from 1 bar to 5 bars results in a 3.96%, 6.54 % and 10.41% decrease in cell efficiency at the BOL, EOL, and after 20,000 h of operation, respectively.

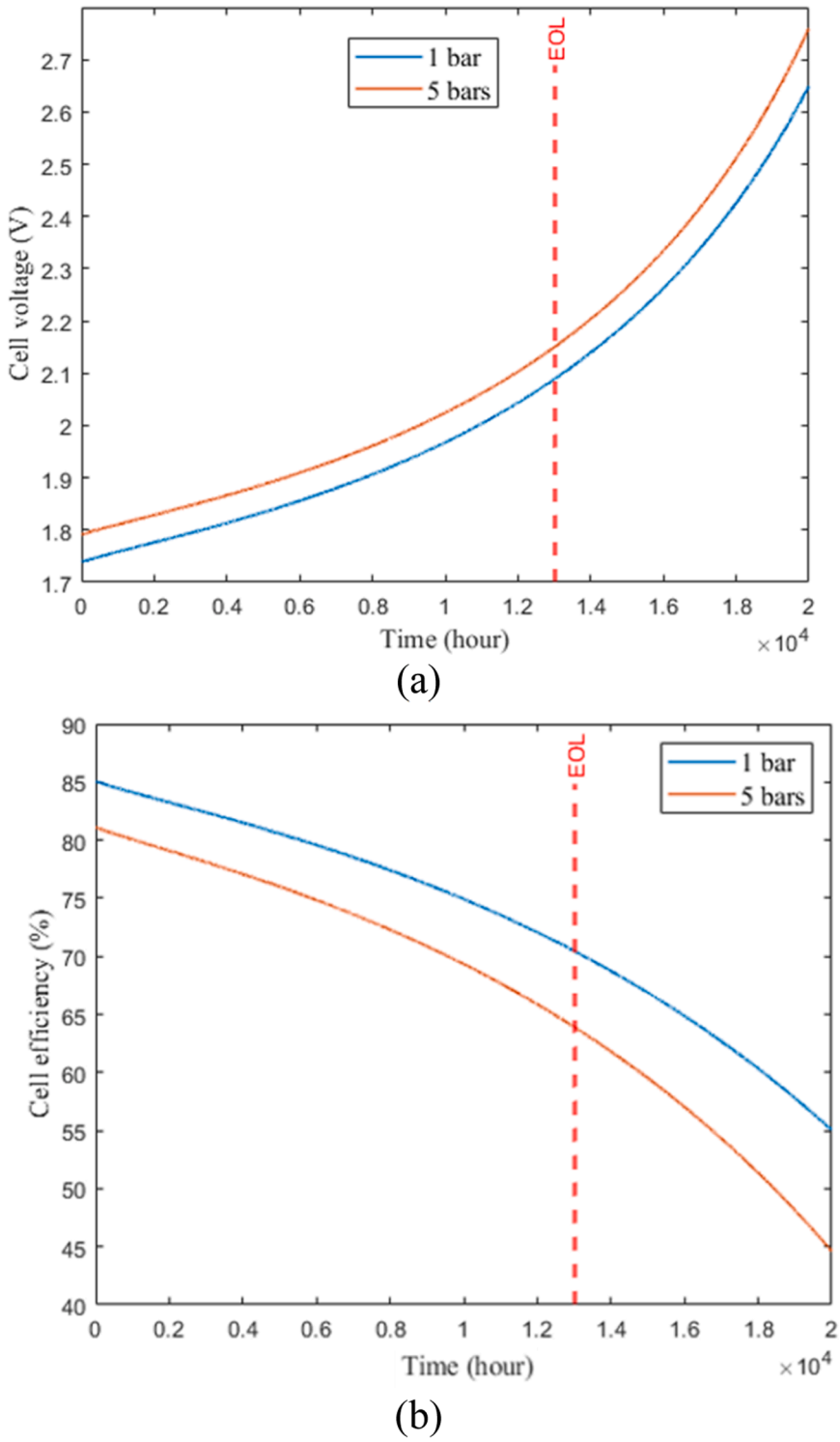

Fig. 25. The impact of operating pressure on (a) cell voltage and (b) energy efficiency of the PEM electrolysis cell over 20,000 h of operation.

3.7. Sensitivity and uncertainty analysis

This section evaluates the impact of plausible variations in the dominant model parameters, including the activation energy of the OER, the fraction of the metal catalyst available at the surface of cathode electrode (ϕ_I), and the membrane water content (λ) on the cell voltage of the pristine cell, the final cell voltage and energy efficiency after 20,000 h of operation, and the EOL. Fig. 26 illustrates that varying the activation energy of the OER, E_A^{OER}, with a baseline value of 21,700 J/mol used in this study, from 10,000–31,700 mol/J, has a negligible effect on the predicted EOL. However, increasing E_A^{OER} within this range leads to a noticeable increase in both the pristine and degraded cell voltages, accompanied by a corresponding decrease in cell efficiency.

Similar to the activation energy of the OER discussed in Fig. 26, the fraction of the metal catalyst available at the surface of the cathode electrode has only a minor influence on the cell voltage of the pristine cell, the cell voltage after 20,000 h of operation, the EOL, and the cell efficiency after 20,000 h of operation, as shown in Fig. 27. According to

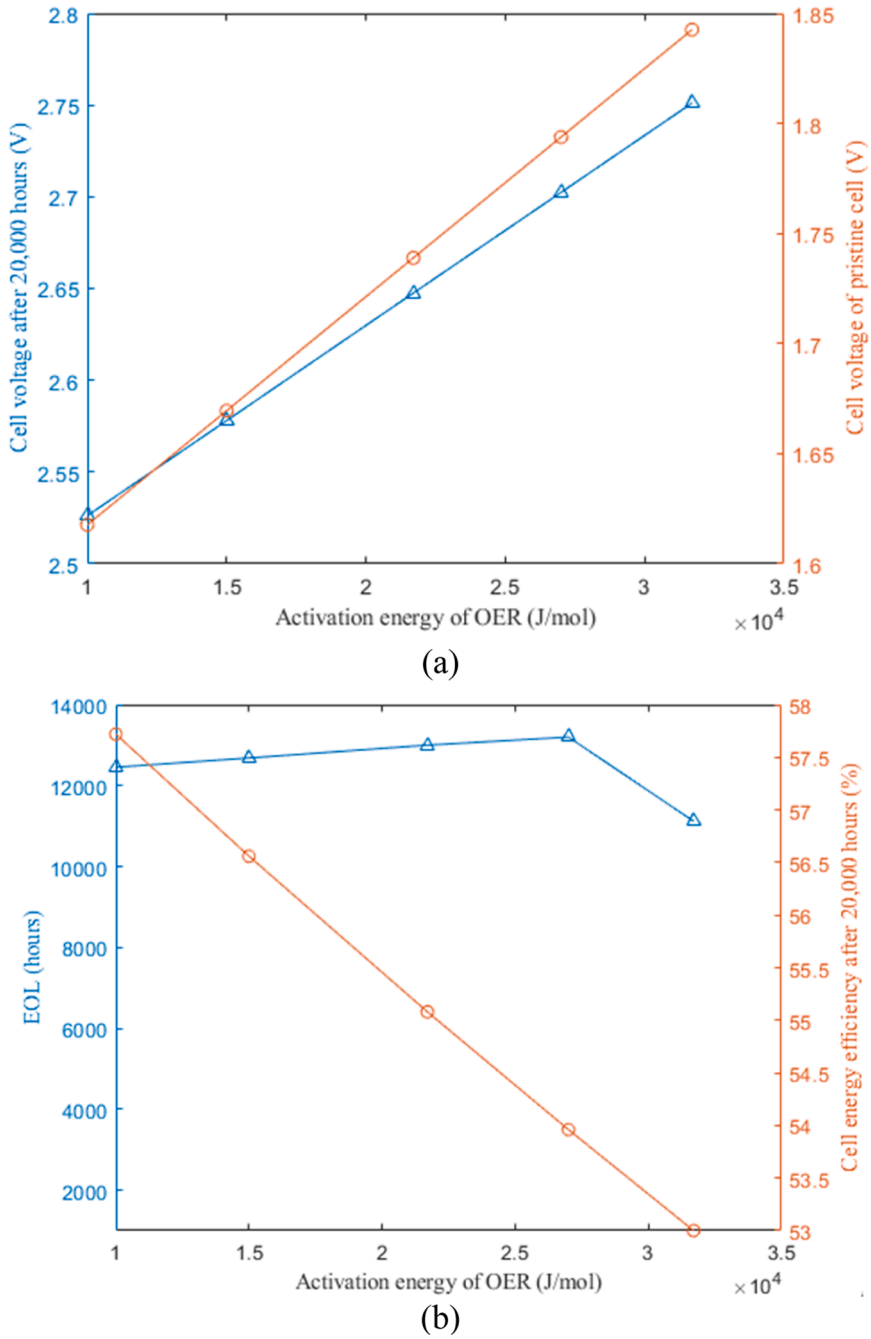

Fig. 26. The impact of varying the activation energy of OER on the (a) cell voltage of pristine cell and degraded cell after 20,000 h (b) EOL and cell energy efficiency after 20,000 h of operation.

the results shown in Fig. 27, varying the fraction of the metal catalyst available at the cathode surface from 0.35 to 0.95, with a baseline value of 0.75 adopted in this study, has a negligible effect on the predicted EOL. Over this range, the pristine cell voltage and the degraded cell voltage after 20,000 h of operation decrease by only 1.55% and 1.11%, respectively, while the cell efficiency after 20,000 h of operation increases by only 0.62%.

Unlike the sensitivity analysis results presented in Figs. 26 and 27, 28 demonstrates that the model predictions are considerably more sensitive to the membrane water content. As shown in Fig. 28, increasing the membrane water content from 14 to 21 results in significant reductions in both the pristine cell voltage and the cell voltage after 20,000 h of operation, by 2.82% and 13.7%, respectively. Under these conditions, the predicted EOL and the cell efficiency after 20,000 h of operation increase by 21.28% and 8.76%, respectively. These results indicate that maintaining a high membrane water content in the membrane not only improves the performance of the pristine cell but also substantially extends the lifetime of the PEM electrolysis cell by mitigating its degradation.

4. Conclusion

This study evaluated the performance of a PEM electrolysis cell and developed a comprehensive model to simulate its performance and degradation over 20,000 h of operation. The analysis considered the primary degradation mechanisms occurring in the CCM, including membrane thinning, platinum crystallite agglomeration on the cathode electrode, and iridium dissolution from the anode catalyst layer. In

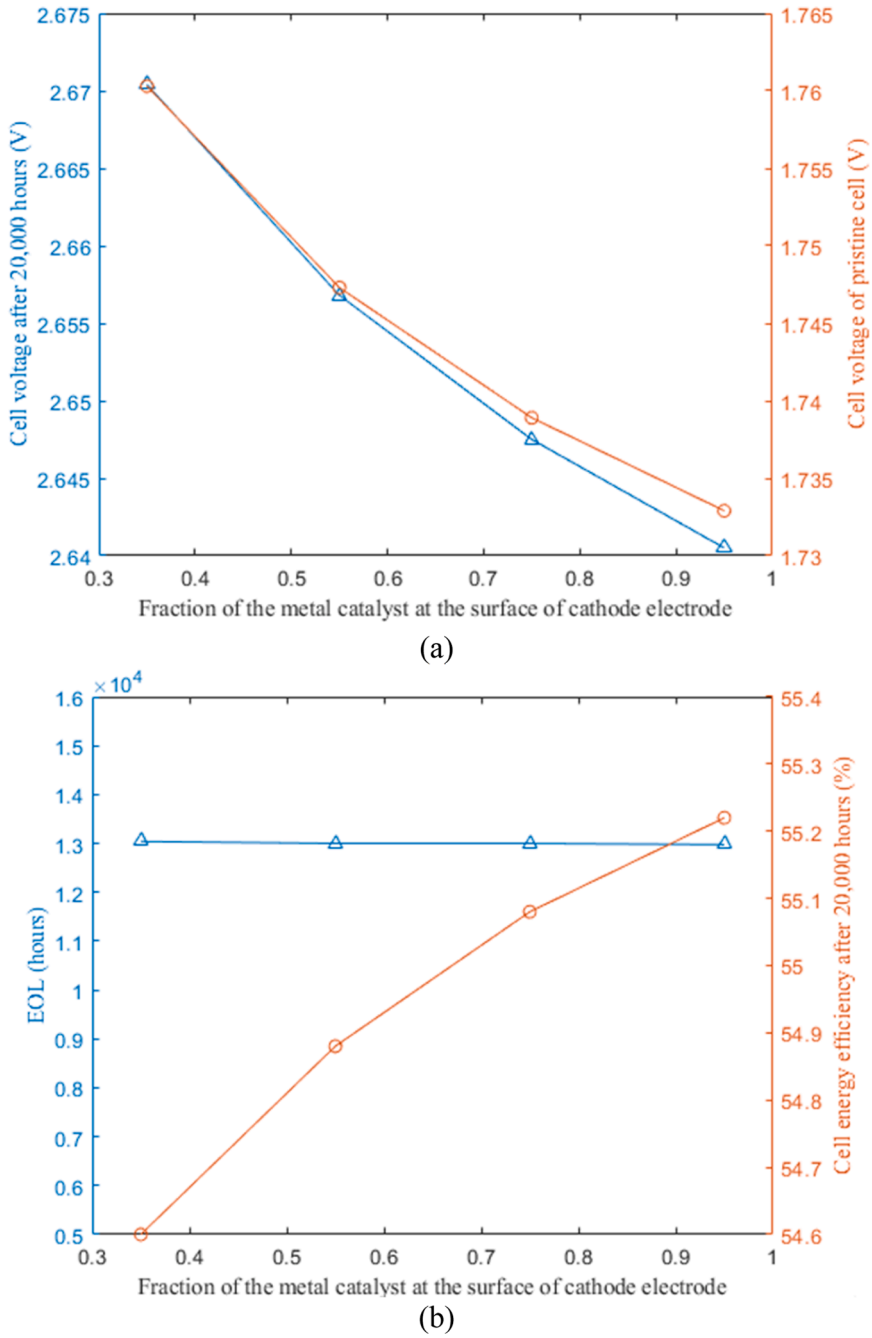

Fig. 27. The impact of varying the fraction of the metal catalyst at the surface of cathode electrode on the (a) cell voltage of pristine cell and degraded cell after 20,000 h (b) EOL and cell energy efficiency after 20,000 h of operation.

addition, hydrogen and oxygen crossovers were investigated in relation to membrane thinning, and the variations in energy efficiency, overpotentials, and cell voltage were quantified for operation at a constant current density of 1 A.cm^{-2} and a temperature of 80 °C. The impact of current density on cell performance was also assessed, along with the effects of LC, idle operation, operating cell temperature and pressure on degradation behavior of the CCM. The main conclusions of this study are as follows:

- Membrane thinning is the dominant degradation mechanism affecting the PEM electrolysis cell performance. It leads to both increased gas crossover and a substantial rise in ohmic overpotential. Specifically, the ohmic overpotential increases from 0.1433 V at BOL to 0.4662 at EOL and to 1.0228 V after 20,000 h of operation at a constant current density of 1 A.cm^{-2}.
- Energy efficiency declines significantly over time, dropping from 85.04 % at BOL to 70.45% at EOL and to 55% after 20,000 h of operation when operating the cell at a current density of 1 A.cm^{-2} and temperature of 80 °C, primarily due to increased ohmic losses associated with membrane thinning.
- Higher current densities adversely affect the performance of the PEM electrolysis cell. While hydrogen production increases with current density as predicted by Faraday's law, ohmic overpotentials and consequently power consumption also rise sharply, resulting in lower energy efficiency. Additionally, operating the cell at elevated current densities leads to higher anodic and cathodic overpotentials, as well

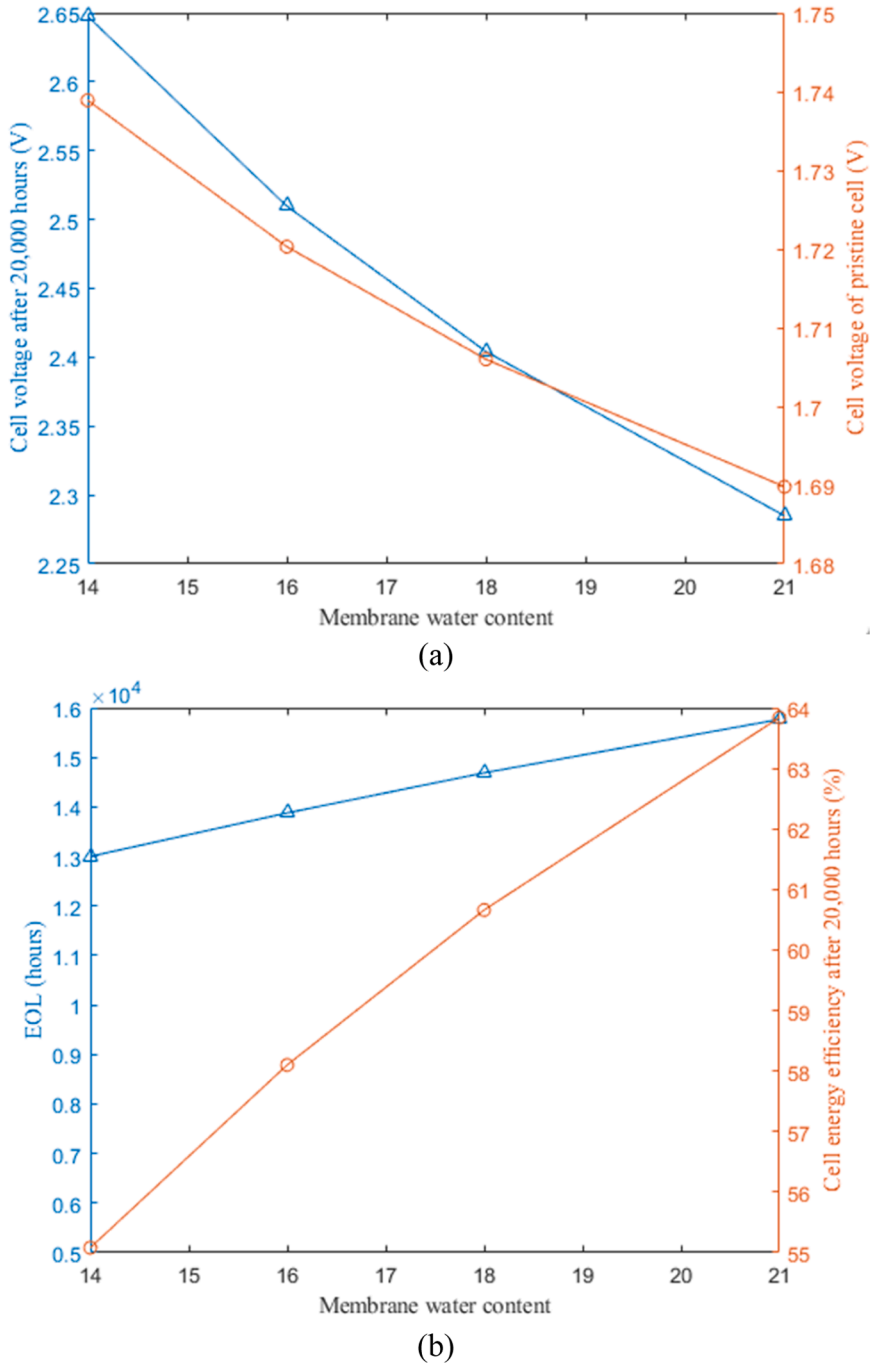

Fig. 28. The impact of varying the membrane water content on the (a) cell voltage of pristine cell and degraded cell after 20,000 h (b) EOL and cell energy efficiency after 20,000 h of operation.

as accelerated anodic degradation rates due to increased iridium dissolution.

- LC has a relatively minor effect on cell degradation. When cycling the current density between 1 A.cm^{-2} to 2 A.cm^{-2} every six hours for five consecutive days, the energy efficiency decreases by only 0.358%, confirming the suitability of PEM electrolysis systems for dynamic operation under variable power supply.
- Operating the cell at higher temperatures reduces overpotentials and improves energy efficiency at BOL but also accelerates the degradation of the electrolysis unit.
- Operating the cell at elevated pressures significantly increases the gas crossover via diffusion, due to the higher partial pressures of hydrogen and oxygen at the cathode and anode, respectively, and their greater solubility in water. This leads to reduced cell energy efficiency, driven by elevated hydrogen crossover and increased cell overpotentials.
- Based on the results of this study, operating the PEM electrolysis cell at 70 °C, 1 A.cm^{-2}, and 1 bar is recommended to achieve a balance between maximizing lifetime (via reduced degradation rates) and maintaining acceptable energy efficiency. It was also demonstrated that, although idle operation decreases the cell lifetime by 12.27%, it may be unavoidable because of the intermittency of renewable energy sources. It should be noted that the observed lifetime reduction associated with frequent idle operation is specific to the operating conditions and idle operation strategy investigated in this study, including an asymmetric pressure configuration (16 bar at the

cathode and atmospheric pressure at the anode), an operating temperature of 80 °C, and an operation cycle consisting of 10 min of idle operation every 20 min, during which the current density decreases from 1 A.cm^{-2} to zero. Therefore, the obtained results should not be generalized to other operating conditions or intermittent operation scenarios.

The degradation mechanisms and the impacts on the electrolysis identified in this work offer valuable guidelines for lifetime prediction and operational strategies for the eventual scale up of the technology in the context of intermittent renewable energy. Future studies may extend the model developed in this study by incorporating simple yet accurate degradation models for the porous transport layers and bipolar plates in the PEM electrolysis cell. The extended model could then be applied to simulate large-scale, MW-capacity stacks while accounting for non-uniform temperature distributions among cells and the effects of current ripples associated with operation under 100% renewable power sources, such as wind and solar energy. In particular, assessing dynamic operation using realistic renewable energy profiles at megawatt scale and developing real-time control-oriented models would provide valuable insights into system degradation mechanisms and optimization strategies for large-scale green hydrogen production. Furthermore, future research can focus on developing data-driven models that integrate mechanistic models with experimental data to provide a realistic overview of cell performance during long-term operation.

CRediT authorship contribution statement

Hossein Asgharian: Writing – original draft, Visualization, Software, Resources, Methodology, Investigation, Formal analysis, Data curation, Conceptualization. **Hamilton Delaney Miller:** Writing – review & editing, Visualization, Software, Data curation, Conceptualization. **Florin Iov:** Writing – review & editing, Supervision, Methodology, Investigation, Conceptualization. **Mads Pagh Nielsen:** Writing – review & editing, Methodology, Investigation, Conceptualization. **Alessandro Hugo Antonio Monteverde:** Writing – review & editing, Resources, Methodology, Formal analysis, Conceptualization. **Vincenzo Liso:** Writing – review & editing, Supervision, Resources, Project administration, Methodology, Investigation, Funding acquisition, Formal analysis, Conceptualization.

Declaration of competing interest

The authors declare that they have no known competing financial interests or personal relationships that could have appeared to influence the work reported in this paper.

Acknowledgment

The authors acknowledge the financial support from ELECTROLIFE project, Grant Agreement Number 101137802.

Supplementary materials

Supplementary material associated with this article can be found, in the online version, at doi:10.1016/j.compchemeng.2026.109892.

Data availability

Data will be made available on request.

References

Awasthi, A., Scott, K., Basu, S., 2011. Dynamic modeling and simulation of a proton exchange membrane electrolyzer for hydrogen production. Int. J. Hydrogen Energy 36 (22), 14779–14786. https://doi.org/10.1016/j.ijhydene.2011.03.045.

Barbir, F., 2005. PEM electrolysis for production of hydrogen from renewable energy sources. Solar Energy 78 (5), 661–669. https://doi.org/10.1016/j.solener.2004.09.003.

Bucci, G., Gadelrab, K., Carter, W.C., 2021. Mesoscale Model for Ostwald Ripening of Catalyst Nanoparticles. J. Electrochem. Soc. 168 (5), 054515. https://doi.org/10.1149/1945-7111/abf970.

Bühre, L.V., et al., 2024. Analysis of Kinetic and Ohmic Resistances in PEM Water Electrolysis through Reference Electrode Measurements. J. Electrochem. Soc. 171 (5), 054518. https://doi.org/10.1149/1945-7111/ad4b5d.

Chandesris, M., Médeau, V., Guillet, N., Chelghoum, S., Thoby, D., Fouda-Onana, F., 2015. Membrane degradation in PEM water electrolyzer: numerical modeling and experimental evidence of the influence of temperature and current density. Int. J. Hydrogen Energy 40 (3), 1353–1366. https://doi.org/10.1016/j.ijhydene.2014.11.111.

Colbertaldo, P., Gómez Aláez, S.L., Campanari, S., 2017. Zero-dimensional dynamic modeling of PEM electrolyzers. Energy Procedia 142, 1468–1473. https://doi.org/10.1016/j.egypro.2017.12.594.

Dam, A.P., Franz, T., Papakonstantinou, G., Sundmacher, K., 2025. Catalyst dissolution in PEM water electrolysis: influence of time, current density and Iridium ion transport in single-pass and recirculation water flow modes. Appl. Catal. B: Environ. Energy 365, 124946. https://doi.org/10.1016/j.apcatb.2024.124946.

De Angelis, S., et al., 2023. Understanding the microstructure of a core–shell anode catalyst layer for polymer electrolyte water electrolysis. Sci. Rep. 13 (1), 1–11. https://doi.org/10.1038/s41598-023-30960-x.

de Groot, M.T., Kraakman, J., Garcia Barros, R.L., 2022. Optimal operating parameters for advanced alkaline water electrolysis. Int. J. Hydrogen Energy 47 (82), 34773–34783. https://doi.org/10.1016/j.ijhydene.2022.08.075.

Dodwell, J., et al., 2021. Open-circuit dissolution of platinum from the cathode in polymer electrolyte membrane water electrolysers. J. Power Sources 498, 229937. https://doi.org/10.1016/j.jpowsour.2021.229937.

Dominguez, D.C., Dam, A.P., Alia, S.M., Richter, T., Sundmacher, K., 2025. Application of a temporal multiscale method for efficient simulation of degradation in PEM Water Electrolysis under dynamic operating conditions. Comput. Chem. Eng. 198, 109083. https://doi.org/10.1016/j.compchemeng.2025.109083.

Escobar-Yonoff, R., Maestre-Cambronel, D., Charry, S., Rincón-Montenegro, A., Portnoy, I., 2021. Performance assessment and economic perspectives of integrated PEM fuel cell and PEM electrolyzer for electric power generation. Heliyon 7 (3), e06506. https://doi.org/10.1016/j.heliyon.2021.e06506.

Fahr, S., Engel, F.K., Rehfeldt, S., Peschel, A., Klein, H., 2024. Overview and evaluation of crossover phenomena and mitigation measures in proton exchange membrane (PEM) electrolysis. Int. J. Hydrogen Energy 68, 705–721. https://doi.org/10.1016/j.ijhydene.2024.04.248.

Ferreira, P.J., et al., 2005. Instability of Pt/C Electrocatalysts in Proton Exchange Membrane Fuel Cells. J. Electrochem. Soc. 152 (11), A2256. https://doi.org/10.1149/1.2050347.

Fouda-Onana, F., Chandesris, M., Médeau, V., Chelghoum, S., Thoby, D., Guillet, N., 2016. Investigation on the degradation of MEAs for PEM water electrolysers part I: effects of testing conditions on MEA performances and membrane properties. Int. J. Hydrogen Energy 41 (38), 16627–16636. https://doi.org/10.1016/j.ijhydene.2016.07.125.

Frensch, S.H., Fouda-Onana, F., Serre, G., Thoby, D., Araya, S.S., Kær, S.K., 2019. Influence of the operation mode on PEM water electrolysis degradation. Int. J. Hydrogen Energy 44 (57), 29889–29898. https://doi.org/10.1016/j.ijhydene.2019.09.169.

García-Salaberri, P.A., et al., 2025. The critical role of the anode porous transport layer/catalyst layer interface of polymer electrolyte membrane water electrolyzers: a parametric analysis. Chem. Eng. J. 509, 160722. https://doi.org/10.1016/j.cej.2025.160722 no. February.

Geuß, M., et al., 2024. Quantification of iridium dissolution at water electrolysis relevant conditions using a gas diffusion electrode half-cell setup. ACS Catal 14 (15), 11819–11831. https://doi.org/10.1021/acscatal.4c02159.

Gladik, A., Riedel, M., Eichel, R.-A., 2025. Intermittent operation of an anion exchange membrane electrolysis system — Unraveling shutdowns as an underestimated risk for degradation. Int. J. Hydrogen Energy 165, 150793. https://doi.org/10.1016/j.ijhydene.2025.150793.

Grigoriev, S.A., Dzhus, K.A., Bessarabov, D.G., Millet, P., 2014. Failure of PEM water electrolysis cells: case study involving anode dissolution and membrane thinning. Int. J. Hydrogen Energy 39 (35), 20440–20446. https://doi.org/10.1016/j.ijhydene.2014.05.043.

Haoran, C., Xia, Y., Wei, W., Yongzhi, Z., Bo, Z., Leiqi, Z., 2024. Safety and efficiency problems of hydrogen production from alkaline water electrolyzers driven by renewable energy sources. Int. J. Hydrogen Energy 54, 700–712. https://doi.org/10.1016/j.ijhydene.2023.08.324.

Kalinnikov, A.A., Grigoriev, S.A., Bessarabov, D.G., 2023. Numerical analysis of the electrochemical dissolution of iridium catalyst and evaluation of its effect on the performance of polymer electrolyte membrane water electrolyzers. Int. J. Hydrogen Energy 48 (59), 22342–22365. https://doi.org/10.1016/j.ijhydene.2023.03.136.

Kimmel, B., et al., 2025. Investigation of the degradation phenomena of a proton exchange membrane electrolyzer stack by successive replacement of aged components in single cells. ACS Sustain. Chem. Eng. 13 (11), 4330–4340. https://doi.org/10.1021/acssuschemeng.4c07358.

Kuhnert, E., Hacker, V., Bodner, M., 2023a. A Review of Accelerated Stress Tests for Enhancing MEA Durability in PEM Water Electrolysis Cells. Int. J. Energy Res. 2023, 1–23. https://doi.org/10.1155/2023/3183108.

Kuhnert, E., Heidinger, M., Sandu, D., Hacker, V., Bodner, M., 2023b. Analysis of PEM Water Electrolyzer Failure Due to Induced Hydrogen Crossover in Catalyst-Coated

PFSA Membranes. Membranes (Basel) 13 (3), 348. https://doi.org/10.3390/membranes13030348.
Kumar, S.Shiva, Himabindu, V., 2019. Hydrogen production by PEM water electrolysis – A review. Mater. Sci. Energy Technol. 2 (3), 442–454. https://doi.org/10.1016/j.mset.2019.03.002.
Lebbal, M.E., Lecœuche, S., 2009. Identification and monitoring of a PEM electrolyser based on dynamical modelling. Int. J. Hydrogen Energy 34 (14), 5992–5999. https://doi.org/10.1016/j.ijhydene.2009.02.003.
Liso, V., Savoia, G., Araya, S.S., Cinti, G., Kær, S.K., 2018. Modelling and experimental analysis of a polymer electrolyte membrane water electrolysis cell at different operating temperatures. Energies (Basel) 11 (12), 3273. https://doi.org/10.3390/en11123273.
Liu, Q., Wang, Y., Liang, X., Chen, H., Zou, X., 2025. Multiscale engineering of anode catalyst layers in proton exchange membrane water electrolyzers. Mater. Chem. Front. 9 (1), 30–44. https://doi.org/10.1039/D4QM00842A.
Medina, P., Santarelli, M., 2010. Analysis of water transport in a high pressure PEM electrolyzer. Int. J. Hydrogen Energy 35 (11), 5173–5186. https://doi.org/10.1016/j.ijhydene.2010.02.130.
Milosevic, M., et al., 2026. Experimental-modeling framework to unveil iridium degradation pathways during intermittent operation in PEMWE. Joule 10 (3), 102309. https://doi.org/10.1016/j.joule.2025.102309.
Minnah, P., Pope, K., 2026. Degradation modelling and the impact of intermittent operation on proton exchange membrane electrolyzers. Int. J. Hydrogen Energy 202, 152962. https://doi.org/10.1016/j.ijhydene.2025.152962.
Onda, K., Murakami, T., Hikosaka, T., Kobayashi, M., Notu, R., Ito, K., 2002. Performance Analysis of Polymer-Electrolyte Water Electrolysis Cell at a Small-Unit Test Cell and Performance Prediction of Large Stacked Cell. J. Electrochem. Soc. 149 (8), A1069. https://doi.org/10.1149/1.1492287.
"Ostwald–Freundlich equation." [Online]. Available: https://en.wikipedia.org/wiki/Ostwald–Freundlich_equation.
Padgett, E., et al., 2025. Quantifying sources of voltage decay in long-term durability testing for PEM water electrolysis. J. Electrochem. Soc. 172 (5), 054508. https://doi.org/10.1149/1945-7111/add184.
Panchenko, O., et al., 2019. Influence of Stoichiometry on the Two-Phase Flow Behavior of Proton Exchange Membrane Electrolyzers. Energies (Basel) 12 (3), 350. https://doi.org/10.3390/en12030350.
Paulsen, M.M., Petersen, S.B., Lozano, E.M., Pedersen, T.H., 2024. Techno-economic study of integrated high-temperature direct air capture with hydrogen-based calcination and Fischer–Tropsch synthesis for jet fuel production. Appl. Energy 369, 123524. https://doi.org/10.1016/j.apenergy.2024.123524.
Rakousky, C., et al., 2017. Polymer electrolyte membrane water electrolysis: restraining degradation in the presence of fluctuating power. J. Power Sources 342, 38–47. https://doi.org/10.1016/j.jpowsour.2016.11.118.
Rakousky, C., Reimer, U., Wippermann, K., Carmo, M., Lueke, W., Stolten, D., 2016. An analysis of degradation phenomena in polymer electrolyte membrane water electrolysis. J. Power Sources 326, 120–128. https://doi.org/10.1016/j.jpowsour.2016.06.082.
Rogler, M., Wagner, R., Thiele, S., Suermann, M., 2025. Guidance for targeted degradation analysis of OER kinetics of low-loading iridium-based catalysts in PEM water electrolysis cells. Electrochim. Acta 510, 145360. https://doi.org/10.1016/j.electacta.2024.145360.
Saidi, S., Brahim, T., Rejeb, O., Jemni, A., 2025. Electrochemical and thermodynamic modeling of PEM electrolyzer performance: a comparative study with and without diffusion overpotential. Int. J. Hydrogen Energy 128, 697–712. https://doi.org/10.1016/j.ijhydene.2025.04.182.
Schalenbach, M., Carmo, M., Fritz, D.L., Mergel, J., Stolten, D., 2013. Pressurized PEM water electrolysis: efficiency and gas crossover. Int. J. Hydrogen Energy 38 (35), 14921–14933. https://doi.org/10.1016/j.ijhydene.2013.09.013.
Siracusano, S., Baglio, V., Van Dijk, N., Merlo, L., Aricò, A.S., 2017. Enhanced performance and durability of low catalyst loading PEM water electrolyser based on a short-side chain perfluorosulfonic ionomer. Appl. Energy 192, 477–489. https://doi.org/10.1016/j.apenergy.2016.09.011.
R. Sorace, "Development and analysis of proton exchange water electrolyzer (PEMWE) Model with chemical degradation phenomenon," 2021, [Online]. Available: https://ntnuopen.ntnu.no/ntnu-xmlui/handle/11250/2781233.
W. Sparber et al., "Strategic Research and Innovation Agenda for RHC, 2013," *Unpublished*, 2013, doi: 10.13140/2.1.4252.7520.
R. Stull, "Vapor Pressure at Saturation." [Online]. Available: https://geo.libretexts.org/Bookshelves/Meteorology_and_Climate_Science/Practical_Meteorology_%28Stull%29/04%3A_Water_Vapor/4.00%3A_Vapor_Pressure_at_Saturation?utm_source=chatgpt.com.
Su, Z., Liu, J., Li, P., Liang, C., 2024. Study of the durability of membrane electrode assemblies in various accelerated stress tests for proton-exchange membrane water electrolysis. Materials (Basel) 17 (6), 1331. https://doi.org/10.3390/ma17061331.
Tejera, G., Rojas, R., Teliz, E., Diaz, V., 2024. PEM electrolysis: degradation study of N1110 assemblies for the production of green hydrogen. Electrochim. Acta 500, 144716. https://doi.org/10.1016/j.electacta.2024.144716.
Tian, Y., et al., 2022. Progress and potential for symmetrical solid oxide electrolysis cells. Matter 5 (2), 482–514. https://doi.org/10.1016/j.matt.2021.11.013.
Valverde-Isorna, L., Ali, D., Hogg, D., Abdel-Wahab, M., 2016. Modelling the performance of wind–hydrogen energy systems: case study the Hydrogen Office in Scotland/UK. Renew. Sustain. Energy Rev. 53, 1313–1332. https://doi.org/10.1016/j.rser.2015.08.044.
Wang, C.R., et al., 2025. Proton Exchange Membrane (PEM) water electrolysis: cell-level considerations for gigawatt-scale deployment. Chem. Rev. 125 (3), 1257–1302. https://doi.org/10.1021/acs.chemrev.3c00904.
Wang, J., et al., 2025. Comparative experimental study of alkaline and proton exchange membrane water electrolysis for green hydrogen production. Appl. Energy 379, 124936. https://doi.org/10.1016/j.apenergy.2024.124936.
Xing, Y., Li, H., Avgouropoulos, G., 2021. Research progress of proton exchange membrane failure and mitigation strategies. Materials (Basel) 14 (10), 2591. https://doi.org/10.3390/ma14102591.
Xu, Y., Cai, S., Chi, B., Tu, Z., 2024. Technological limitations and recent developments in a solid oxide electrolyzer cell: a review. Int. J. Hydrogen Energy 50, 548–591. https://doi.org/10.1016/j.ijhydene.2023.08.314.
Yodwong, B., Guilbert, D., Phattanasak, M., Kaewmanee, W., Hinaje, M., Vitale, G., 2020. Faraday's efficiency modeling of a proton exchange membrane electrolyzer based on experimental data. Energies (Basel) 13 (18), 4792. https://doi.org/10.3390/en13184792.
Zhao, Z., Li, S., Xiong, C., Cui, P., Wang, S., Zhang, A.-M., 2025. New insights into the cavitation erosion by bubble collapse at moderate stand-off distances. J. Fluid Mech. 1015, A33. https://doi.org/10.1017/jfm.2025.10331.